CHAPTER 9

# Surface Energy Budget and Fuel Moisture

KENNETH E. KUNKEL
*Illinois State Water Survey, Champaign, Illinois*



*Forest Fires*

# I. INTRODUCTION

The effect of weather on fuel moisture has traditionally been estimated using statistically based empirical relationships that are a function of temperature and relative humidity (Simard, 1968; Van Wagner, 1987). These relationships have provided a useful approach to estimate the danger of forest fires. However, because they are not based on fundamental physical principles, it may not always be appropriate to use them as a tool to study fuel-drying processes. There is no assurance that these relationships will hold in a general sense. In fact, the differences in systems of Canada, the United States, and other countries suggests that any particular set of these relationships may not be generally applicable to the other regions. In Chapter 4 in this book, a detailed description of the principles governing moisture within fuels is provided. This chapter builds on that discussion by describing the broadly applicable physical principles of evaporation as it relates to fuel drying. It is hoped that this information can be used by the ecological researcher to more accurately describe the fuel conditions that are encountered in field studies and to identify the important processes and mechanisms responsible for those fuel conditions.

The moisture content of forest fuels is dependent on a number of factors. This chapter will examine the meteorological factors that influence variations in fuel moisture content. Specifically, the meteorological factors that affect evaporation rates are discussed in detail. A number of methods for estimating evaporation rates are described, with a primary emphasis on the widely used Penman-Monteith formulation. This formulation is used to describe the functional dependence of evaporation rates on important meteorological variables. Also, the state of the atmosphere in close proximity to the Earth's surface and its importance to the environmental conditions experienced by fuels are discussed. Finally, the chapter discusses state-of-the-art models that are used in atmospheric circulation models to describe the complex interactions between the land surface and the atmosphere. Such models may be of use to the ecological researcher in describing evaporative drying of fuels.

In living fuels, foliage and twigs play an important role in forest fire behavior and can exhibit significant fluctuations in moisture content (Chandler *et al.*, 1983). The moisture content is determined by the relative balance between evaporative losses and supply of water from the root system. Water is lost through transpiration, which is controlled by meteorological factors and the degree of stomatal opening. Water uptake by the roots is controlled by soil characteristics, soil moisture content, and the vertical distribution of roots. When soil moisture is high, water loss is approximately balanced on a daily time scale by water uptake. When soil moisture is deficient, root uptake of water is restricted and may not balance transpiration losses, leading to gradual decreases

in fuel moisture content. The diurnal cycle of transpiration is of large amplitude, peaking in early afternoon, and this leads to changes in fuel moisture content during the day (Chandler *et al.*, 1983).

The moisture content of dead fuels is controlled by different processes (Pyne, 1984), although a similar set of meteorological factors provide the atmospheric control on these processes. Moisture cannot be replenished by root uptake. Moisture replenishment can occur by absorption through direct contact with liquid water. Moisture exchange in the gaseous phase depends on the fuel's hygroscopic properties and is driven by the difference in water vapor pressure between the fuel particle interior and the atmosphere in immediate contact with the fuel. Fine fuels, such as grass, leaves, needles, and ground litter, can rapidly change moisture content over time scales of hours. Medium (sticks, branches) and coarse (logs) fuels change moisture more slowly, on time scales of weeks to months for medium fuels and months to years for coarse fuels (Brown and Davis, 1973). For these fuels, the persistence of meteorological conditions is an important factor in determining fire risk.

## II. EVAPOTRANSPIRATION PROCESSES AND THE METEOROLOGICAL CONTROLLING FACTORS

The evaporation of water from the soil or from the surface of living or dead fuels or the transpiration of water through leaves will be referred to herein by the common term "evapotranspiration" (ET). Fundamentally, ET can occur when the water vapor pressure of the air layer immediately adjacent to the surface containing liquid water is lower than the water vapor pressure of the liquid water. If the adjacent air layer and liquid water surface are in thermal equilibrium (often the case), then ET can occur when the water vapor pressure of the adjacent air layer is below its saturated value. The saturation water vapor pressure is a function of temperature.

The latent heat of vaporization of water is high, with a value of 2454 J $g^{-1}$ at 20°C, varying slightly with temperature. The rate of ET is often limited by availability of energy. In a closed system, an unsaturated near-surface air layer will be moistened and cooled by ET and quickly reach saturation, stopping the process of ET. In the atmosphere, ET is sustained principally by two processes. The first process is the absorption of electromagnetic radiation at the surface, which raises the temperature of the liquid water and the adjacent air. Thus, the value of saturation of the adjacent air is increased, in essence increasing the capacity of the air for further evaporation. The second process is ventilation of the surface–air interface, which replaces the moistened air near the interface with

drier and/or warmer air. Several meteorological variables are of particular importance in determining the magnitude of these two processes. These are shortwave and longwave radiation, temperature, atmospheric water vapor content, and vertical mixing.

## A. Radiation

The primary source of energy for ET is electromagnetic radiation from the sun which is concentrated principally in the visible and near-infrared (shortwave) portion of the spectrum, at wavelengths less than $3 \times 10^{-6}$ m. The amount of radiation that is available for ET is determined by several processes, as described later.

The amount of incoming solar radiation at the top of the atmosphere varies with latitude and season based on the Earth–sun geometry. Solar radiation is attenuated as it passes through the atmosphere by direct absorption and scattering by gases, particulates, and, most importantly, clouds. Globally averaged, about 54% of the solar energy at the top of the atmosphere reaches the Earth's surface (Salby, 1996). At the surface, some of the solar radiation is reflected back to space. The reflectivity of the surface varies considerably with surface type and is represented by a parameter called the albedo, which is the fractional part of the radiation that is reflected. Except for snow-covered surfaces, the albedo of most surfaces is less than 0.3. For example, Betts and Ball (1997), in the BOREAS experiment (Sellers *et al.*, 1997), measured summertime albedos of 0.20 over grass, 0.15 over an aspen forest, and 0.083 over a coniferous forest.

The rate of emission of radiation by matter is governed by the Stefan-Boltzmann law,

$$I = \varepsilon \sigma T^4 \tag{1}$$

where $I$ = energy flux (W m$^{-2}$), $\varepsilon$ = emissivity, $\sigma$ = Stefan-Boltzmann constant ($5.67 \times 10^{-8}$ W m$^{-2}$ K$^{-4}$), and $T$ = temperature of the matter (K). At the range of temperatures of the atmosphere and the earth's surface, this emission is in the infrared (longwave) portion of the spectrum, mostly at wavelengths $>3 \times 10^{-6}$ m. Most land surface types have high emissivities, with forests in the range of 0.97–0.99 (Oke, 1978). Although the cloud-free atmosphere is nearly transparent at visible wavelengths, it is semiopaque at infrared wavelengths and absorbs and reemits a significant amount of infrared radiation toward the surface. The magnitude of infrared radiation emitted by the cloud-free atmosphere is largely determined by the temperature and water vapor content in the lowest portion of the atmosphere. However, clouds have a much higher emissivity than the cloud-free atmosphere. Thus, the amount and type of cloud cover is an important factor in determining the magnitude of atmospheric in-

frared radiation. The upward longwave radiation, $I_s$, above the Earth's surface is the sum of the emission by the Earth's surface, governed by Eq. (1), and the reflection of downward longwave radiation from the atmosphere, $I_a$. Usually, the absorptivity (1 − reflectivity) of the Earth's surface is assumed to be equal to the emissivity. Thus,

$$I_s = \varepsilon_s \sigma T_s^4 + (1 - \varepsilon_s) I_a \tag{2}$$

where $\varepsilon_s$ = emissivity of the surface and $T_s$ = temperature of the surface (K).

A portion of the electromagnetic radiation that reaches the Earth's surface is transformed into nonradiative forms of energy, including latent heat through the ET process, heat storage in the soil and biomass, and direct heating of the atmosphere through conduction. The amount of radiation available for transformation into these other forms of energy is called the net radiation ($R_n$) and is defined as

$$R_n = S_d(1 - a) + I_a - I_s \tag{3}$$

where $S_d$ = downward solar radiation at the Earth's surface (W m$^{-2}$) and $a$ = albedo. Figure 1 shows the diurnal evolution of $R_n$ on a typical sunny summer day in the central United States, along with the individual components in Eq. (3), as measured by a SURFRAD station (see discussion that follows). There is a strong diurnal dependence to $R_n$, with the magnitude peaking near midday and dropping to negative values at night, primarily in response to the

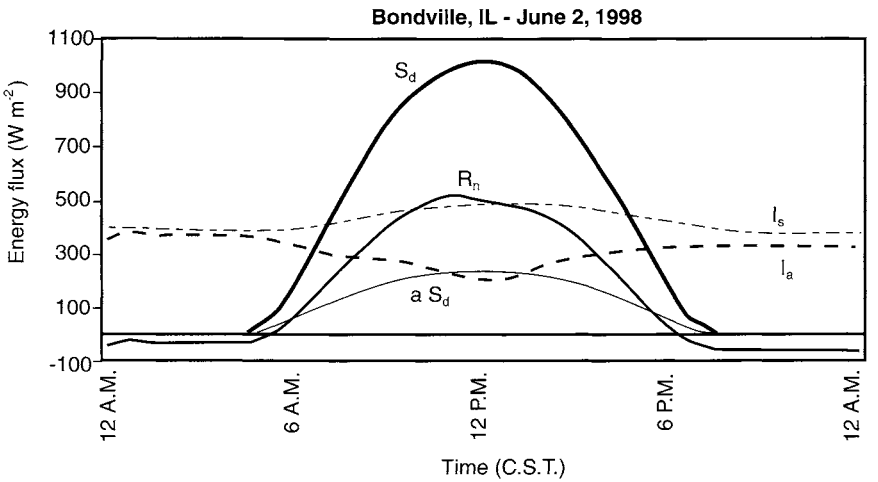


FIGURE 1 Daily variation in the components of the surface radiation budget at the SURFRAD site at Bondville, Illinois, on June 2, 1998. Components are $R_n$ (medium solid), $S_d$ (thick solid), $aS_d$ (thin solid), $I_s$ (thin dashed), and $I_a$ (thick dashed).

variation of incoming solar radiation. Infrared radiation ($I_s$, $I_a$) also varies through the day, although with a lesser amplitude than solar radiation.

The daily accumulated radiative energy available to be transformed into other forms of energy, found by integrating $R_n$, is positive in Figure 1. The magnitude of the daily integrated $R_n$ varies with latitude, the seasonal cycle, and meteorological conditions (particularly cloud cover). However, the climatology of $R_n$ is not well specified because the measurement of $R_n$ is technically difficult; data have typically been obtained only for short duration field experiments. Even in carefully controlled experiments, commercially available sensors have been found to exhibit biases (Hodges and Smith, 1997). To address the need for climatic observations of radiation, the Surface Radiation Budget Network (SURFRAD) was established in the United States in 1993 by the U.S. Department of Commerce's National Oceanic and Atmospheric Administration. The SURFRAD is providing accurate, long-term, continuous measurements of the surface energy budget at six sites in climatologically diverse regions of the United States. Figure 2 shows the annual cycle in 1997 of the daily average values of the radiation budget components at Goodwin Creek, Mississippi. All components exhibit a pronounced seasonal cycle, with values peaking in the summer. Daily $R_n$ peaks at about 13 MJ $m^{-2}$ in July and falls to a minimum of less than 2 MJ $m^{-2}$ in December. Daily integrated values of $I_a$ and $I_s$ are much higher than $S_d$ because infrared radiation occurs at night as well as during day. However, these largely cancel, and the net infrared radiation ($I_a - I_s$) is smaller than the net shortwave radiation throughout the year.

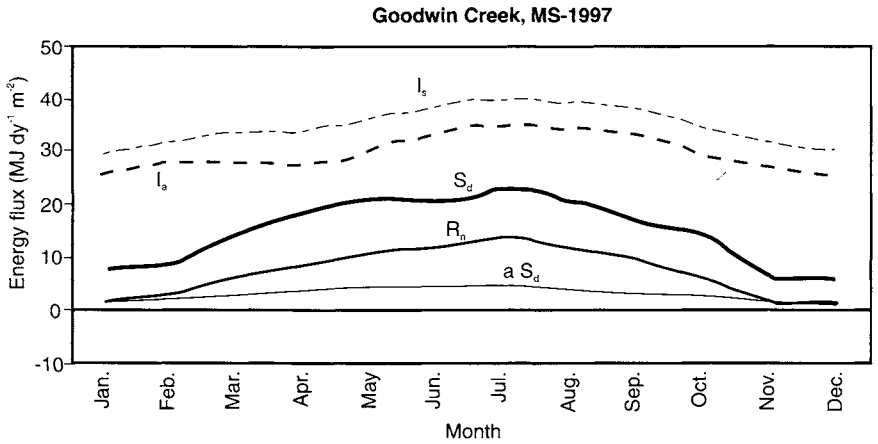


FIGURE 2 Annual cycle of the daily average values of the components of the surface energy budget at Goodwin Creek, Mississippi, during 1997. Components are $R_n$ (medium solid), $S_d$ (thick solid), $aS_d$ (thin solid), $I_s$ (thin dashed), and $I_a$ (thick dashed).

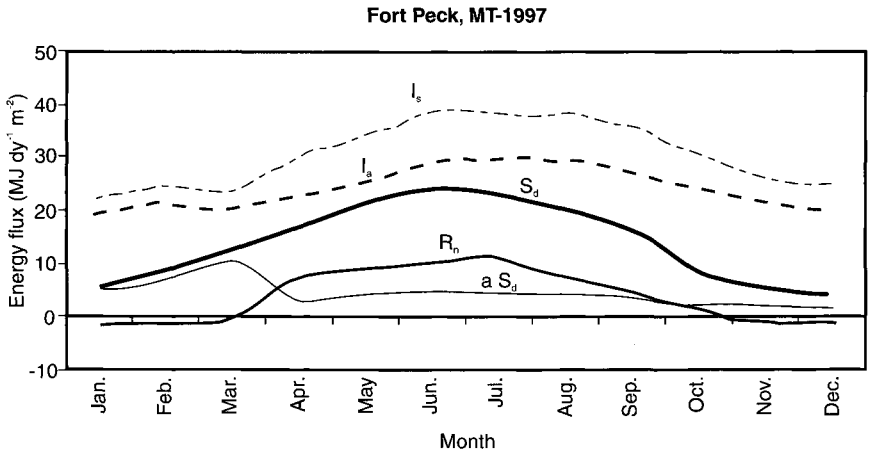


FIGURE 3 Annual cycle of the daily mean values of the surface energy budget components during 1997 at Fort Peck, Montana. Components are $R_n$ (medium solid), $S_d$ (thick solid), $aS_d$ (thin solid), $I_s$ (thin dashed), and $I_a$ (thick dashed).

Figure 3 shows the radiation components for a more northern location: Ft. Peck, Montana. The seasonal cycle is qualitatively similar, but there are some significant differences. Incoming solar radiation peaks in summer at about 24 MJ $m^{-2}$, slightly higher than in Mississippi. This is a consequence of longer days and lower cloud cover at Ft. Peck, which offsets the higher solar elevation angles at Goodwin Creek. The amplitude of the annual cycle is higher at the more northern Montana location. The rather high values of reflected solar radiation ($aS_d$) in January, February, and March, reaching a peak of about 10 MJ $m^{-2}$ in March, are a result of snow cover and the high albedo associated with snow cover. The peak value of $R_n$ in summer is lower in Montana than in Mississippi. A comparison of Figures 2 and 3 indicates that this is primarily a result of lower values of incoming longwave radiation at the Montana site, probably due to lower water vapor content and lower air temperatures. During the cold season, net radiation is negative at Ft. Peck due to high values of reflected shortwave radiation.

There are no comparable long-term SURFRAD sites over a forest canopy. However, short-term experiments indicate that the radiation budget over a forest canopy is qualitatively similar to what is shown in Figures 2 and 3. For example, McCaughey *et al.* (1997) measured the longwave components of the surface energy budget over a jack pine (*Pinus banksiana*) forest in Saskatchewan, Canada, during the warm season. Net longwave radiation was very similar to what is seen in Figure 3 for Fort Peck, Montana.

At ground level within a forest canopy, net radiation is reduced sharply below that at the top of the canopy because of shielding by the canopy. The magnitude of the reduction in $R_n$ depends upon tree density, tree architecture, and the season. J. M. Chen *et al.* (1997) measured net radiation in a relatively sparse aspen (*Populus tremuloides*) forest. Net radiation at ground level was about half of the above-canopy value before leaf emergence and about a quarter of the above-canopy value after leaf emergence. Baldocchi and Vogel (1996) measured net radiation in a deciduous forest and a boreal jack pine (*Pinus banksiana*) forest. Net radiation at the forest floor in the deciduous forest was less than 10% of the value above the canopy. Net radiation at the floor of the jack pine forest was 10–15% of the above-canopy level. Black and Kelliher (1989) measured net radiation in a Douglas fir (*Pseudotsuga menziesii*) stand and found that below-canopy net radiation was 13–16% of the above-canopy levels. These selected examples suggest that the available energy for evapotranspiration at the forest floor is usually a small fraction of what is available at the top of the canopy.

## B. Atmospheric Water Vapor Content

The saturation value of atmospheric water vapor content is a highly nonlinear function of temperature. This dependence can be expressed as (Buck, 1981)

$$es = A \exp[BT/(C + T)] \tag{4}$$

where $es$ = saturation value of water vapor pressure (hPa), $T$ = temperature (°C), and $A$, $B$, and $C$ are constants. Over water, the values of these constants are $A = 6.1121$, $B = 17.502$, and $C = 240.97$. Over ice, the values are $A = 6.1151$, $B = 22.452$, and $C = 272.55$. A graphical representation of Eq. (4) is shown in Figure 4, over water and over ice. The value of $es$ approximately doubles for every 10°C increase in temperature. At temperatures below 0°C, there are small differences in $es$ over water and over ice.

Evaporation rates in the air layer adjacent to a flat water surface are proportional to the difference $(es - e)$, where $e$ = actual water vapor pressure, when water is freely available and the water surface is in thermal equilibrium with the adjacent air layer. This difference is referred to as the water vapor pressure deficit. Thus, evaporation rates are highly dependent on temperature because of the relationship of $es$ to $T$.

Observations of atmospheric water vapor content are usually expressed in terms of dew point temperature ($T_d$, °C) or relative humidity (RH, %). The actual water vapor pressure ($e$) is related to $T_d$ by

$$e = A \exp[BT_d/(C + T_d)] \tag{5}$$

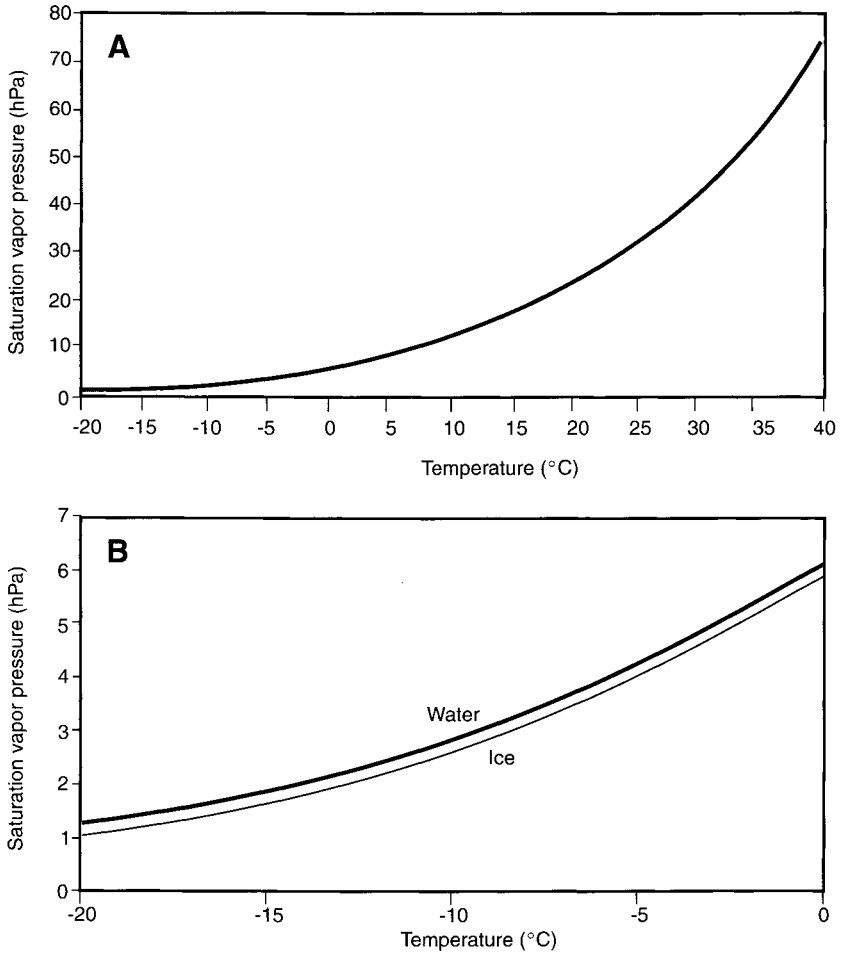


FIGURE 4 Dependence of the saturation water vapor pressure (hPa) on temperature (°C) (A) over water for $T > -20$°C and (B) over water and ice for $T < 0$°C.

Relative humidity is defined in terms of the mixing ratio ($v$), which is the ratio of the mass of water vapor to the mass of dry air in a volume. The definition is

$$\mathrm{RH}\,(T) = 100\%\ v/vs\,(T) \tag{6}$$

where $vs\ (T)$ is the saturation mixing ratio at the air temperature $T$. The relationship of vapor pressure to mixing ratio is (List, 1949)

$$v = 0.62197\ e/(P - e) \tag{7}$$

where $P$ = air pressure (hPa). Relative humidity can then be expressed in terms of vapor pressure as

$$\mathrm{RH} = 100\% \frac{e(P - es)}{es(P - e)} \tag{8}$$

Water vapor content can also be defined as the ratio of the mass of water vapor to the mass of moist air in a volume, known as the specific humidity ($q$). This can be expressed in terms of the mixing ratio as

$$q = v/(1 + v) \tag{9}$$

Relative humidity is strongly dependent on temperature through its dependence on $es$. In most situations, there is little diurnal variation in $e$ but large variations in RH. RH usually reaches a maximum in the early morning around sunrise when temperatures are at a minimum and falls to a minimum in mid afternoon around the time of the daily maximum temperature. This behavior is illustrated by the daily average profile for International Falls, Minnesota, in July (Figure 5). There is relatively little variation in water vapor pressure, ranging from 14.6 hPa in the early morning to 16.4 hPa in late morning, a total percentage change of 11%. By contrast, relative humidity varies from near 90% in the early morning to near 50% in late afternoon.

Some measures of ET use relative humidity as one indicator of drying rates. By itself, RH may be a deceptive indicator because of its dependence on temperature. Figure 6 shows the dependence of the water vapor pressure deficit on

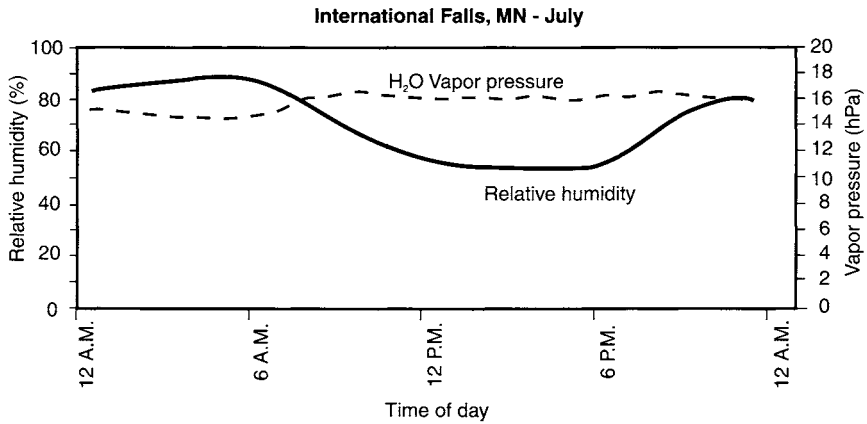


FIGURE 5 The diurnal cycle of relative humidity (%, solid line) and atmospheric water vapor pressure (hPa, dashed line) during July at International Falls, Minnesota. These are averages of hourly observations for the period 1961–1990.

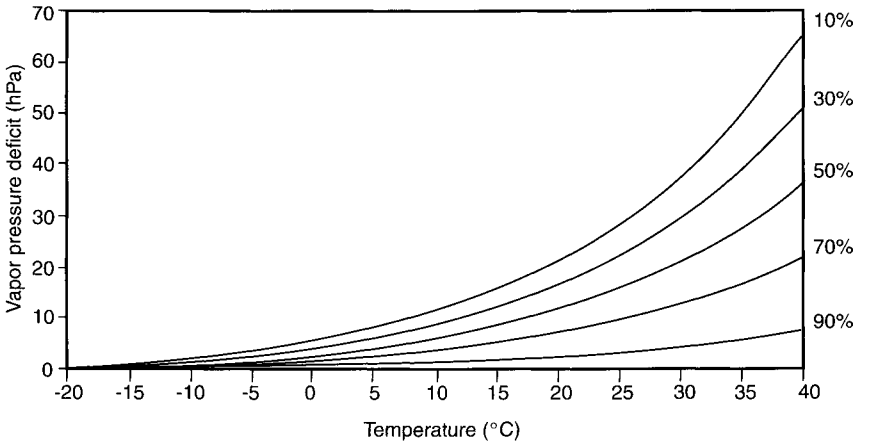


FIGURE 6 The dependence of the water vapor pressure deficit (hPa) on temperature (°C) for relative humidity values of 10, 30, 50, 70, and 90%.

temperature for selected values of relative humidity. The water vapor pressure deficit, and thus the ET rates, increases exponentially with temperature, following Eq. (4), for constant RH.

## C. Temperature

The dependence of evaporation on temperature is primarily through the dependence of *es* on temperature. Temperature may also have indirect effects because longwave radiation increases with temperature. However, as illustrated in Figures 2 and 3, net longwave radiation ($I_a - I_s$) is only weakly dependent on season (temperature).

## D. Vertical Mixing (Wind and Stability)

Evaporation moistens and cools the air near the surface, which has a negative feedback on evaporation rates. Mixing of air near the surface has the net effect of transporting moist air upward and replacing it with drier and/or warmer air from aloft, maintaining evaporation. One factor affecting the rate of mixing is wind speed. Evaporation rates tend to increase with increasing wind speed, other factors being equal. A second factor is the vertical air density gradient which can enhance or suppress mixing.

## 1. Mixing Processes

Mixing in the lowest few meters of the atmosphere is driven primarily by the interaction of the surface with the atmosphere. The Earth's surface is aerodynamically rough and interacts with moving air. This interaction results in the transfer of momentum between the surface and the atmosphere. The wind speed near the surface is reduced by this momentum transfer. Momentum transfer occurs through two processes. The first is friction; air in direct contact with surface elements is slowed by frictional forces. Vertical mixing processes transfer this slow moving air stream upward away from the surface to a region of faster moving air streams and vice versa. This exchange slows the faster moving air and accelerates the slower moving air. The second process is through the pressure force; high-pressure builds up on the windward side of surface elements that are exposed to the wind which then slows the air upwind of the element. This process does not involve exchange of air and momentum is transferred without direct contact with the surface.

Mixing occurs either by molecular diffusion in laminar flow or by turbulence. Momentum transfer to the surface results in a vertical gradient in wind speed. This gradient is often sufficiently large that laminar flow is unstable, and turbulent motion results. Turbulent mixing is much more efficient than molecular diffusion. The atmospheric transport of momentum usually occurs at much higher rates than provided by molecular diffusion because the atmosphere near the surface is generally turbulent, except immediately adjacent to the surface. In a shallow layer (of the order of 1 cm thickness) near surface objects, proximity to the surface prevents turbulent motion and the wind flow is laminar; the transfer of momentum, heat, and water vapor occurs by molecular diffusion in this shallow, laminar-flow layer.

## 2. Atmospheric Stability

The second factor affecting the rate of mixing, in addition to the interaction of the wind with the surface, is the stability of the atmosphere. Because pressure decreases with height, the temperature of a rising parcel of air will decrease with height at a rate known as the "adiabatic lapse rate," as governed by the gas law, whose value is $9.8°C\ km^{-1}$. If temperature decreases with height at a slower rate than adiabatic, then a rising parcel will find itself at a lower temperature (higher density) than the surrounding environment and will tend to sink back to its original level. This suppresses vertical mixing and the atmosphere is referred to as "stable." If the temperature decreases with height more rapidly than adiabatic, then a rising parcel of air will find itself at a higher temperature (lower density) than the surrounding environment and will accelerate upward. This enhances vertical mixing and the atmosphere is referred to as "unstable." It has

been convenient within the science of meteorology to define stability conditions through use of a quantity known as the potential temperature ($\theta$) which is defined as

$$\theta(z) = T(z)\left[\frac{P_0}{P(z)}\right]^{0.287} \tag{10}$$

where $z$ = height, $T(z)$ has units of K, and $P_0$ is the pressure of a reference level, usually taken to be 1000 hPa. In essence, the potential temperature is a value that has been adjusted for the changes in temperature that occur due to pressure changes when a parcel rises or sinks in the atmosphere. When expressed in terms of $\theta$, the criteria for stability become

$$\begin{aligned} \frac{\partial\theta}{\partial z} &< 0 \quad \text{unstable} \\ \frac{\partial\theta}{\partial z} &= 0 \quad \text{neutral} \\ \frac{\partial\theta}{\partial z} &> 0 \quad \text{stable} \end{aligned} \tag{11}$$

In a stable atmosphere, the character of the wind flow, whether turbulent or laminar, is determined by a balance between the tendency for vertically sheared flow to break down into turbulence and the suppression of vertical motions by stable buoyancy. This characteristic is often expressed in a parameter known as the gradient Richardson number (Ri), defined as

$$\text{Ri} = \frac{g}{T}\frac{\partial\theta}{\partial z}\Big/\left(\frac{\partial U}{\partial z}\right)^2 \tag{12}$$

where $g$ = acceleration of gravity, and $U$ = horizontal wind speed. When Ri is greater than about 0.25, turbulent motion ceases, and the flow becomes laminar. In this case, exchange of momentum, heat, and water vapor is markedly reduced. In the opposite case, when the potential temperature decreases with height, the atmosphere is buoyantly unstable, and convection transfers momentum and enhances the rate of turbulent mixing.

The lowest layer of the atmosphere, where turbulence driven by momentum and heat exchange at the surface is present, is often referred to as the planetary boundary layer (PBL). During the daytime, when incoming solar radiation creates an unstable temperature profile, the depth of the PBL is typically 1–2 km (Panofsky and Dutton, 1984). At night, under a stable temperature profile, the PBL depth is often less than 100 m, particularly when the wind speed is low. The lowest part of the PBL is referred to as the surface layer. The surface layer is not precisely defined; within this layer, vertical variations of momentum, heat, and

moisture fluxes are small (<10%) and, as a first approximation, can be assumed to be constant with height. As a rule of thumb, the surface layer occupies the lowest 10% of the PBL (Panofsky and Dutton, 1984).

## 3. Vertical Wind Profile

The turbulent transport of momentum between the surface and the atmosphere creates a vertical gradient in wind speed. Within the surface layer, the wind speed typically increases with the logarithm of height, as documented by numerous field experiments. Mathematically, the wind speed ($U$) dependence on height ($z$) can be expressed as (Panofsky and Dutton, 1984)

$$U(z) = \frac{u_*}{k}\{\ln[(z - d)/z_0] - \psi_m\} \tag{13}$$

where $u_*$ = the friction velocity (m s$^{-1}$), $d$ = displacement height (m), $z_0$ = roughness length (m), $k$ = von Karman constant (= 0.4), and $\psi_m$ is a correction factor for stability effects. The friction velocity is a measure of the rate of momentum transport. The displacement height is a measure of the shielding of the Earth's surface by a vegetative canopy. For short grass and short crops, $d$ is small or negligible. However, a dense forest canopy is very effective at shielding the free atmospheric flow from the surface; from the viewpoint of the atmosphere, the effective surface is much higher than the actual ground level. Typically, in dense crops or forests, the displacement height is 60–80% of the average height of the vegetation (Thom, 1975).

The roughness length is a measure of the efficiency of the interactions between the free atmospheric flow and the surface. For a very smooth, flat surface, such as a sandy desert, the interaction between the free atmospheric flow and the surface is minimal, and the corresponding roughness length of that surface is also small. By contrast, surfaces that have many undulations which provide opportunities for airflow to penetrate between the undulations and be slowed by interactions with these undulations are much more efficient at transferring momentum and the corresponding roughness length is much larger. Forests typically have rather large roughness lengths because of the tall trees that comprise the forest and the many openings that allow air to penetrate into the forest canopy. Interestingly, very dense forests where air cannot penetrate readily down into the canopy can have a smaller roughness length than a more open forest where the wind flow can more easily penetrate deeper into the canopy. In general, the roughness length is a function of the height of the surface roughness elements, their density, and their flexibility. The roughness length in general will increase with increasing height of the surface elements. The roughness length will also increase with the increasing density of the surface elements up to a point above which the roughness length will decrease as the density be-

comes very high. Also the roughness length generally decreases with increasing flexibility of vegetation, since the pressure force mechanism for momentum transport will be more effective for rigid objects than for flexible objects. As roughness increases, turbulence and vertical mixing rates increase. Garratt (1977) and Oke (1978) provide typical values of $z_0$ for a wide range of surfaces. Forests have values usually in the range of 1–6 m. By contrast, the roughness height of short grass is of the order of 1 cm.

The logarithmic wind profile applies to the free atmosphere above the canopy. Within the canopy, the vertical wind speed gradient is dependent on the structure and density of the canopy (Fritschen, 1985). Denser canopies are characterized by lower wind speeds than more open canopies. The gradient within the canopy has often been parameterized with an exponential function (Cionco, 1965):

$$U(z) = U(h) \exp[\beta(1 - z/h)] \tag{14}$$

where $h$ = height of the canopy, and $\beta$ is a parameter called the wind velocity attenuation coefficient. For forest canopies, $\beta$ is typically in the range of 2–5 (Cionco, 1978). These values of $\beta$ indicate that wind speeds at the floor of a forest are a small fraction of values at the top of a forest, thus reducing ventilation and ET rates.

Water vapor is to a first approximation a passive element in the surface mixing process. When momentum is transported through friction, in which slow-moving air molecules near surface objects are exchanged with faster moving air, water vapor molecules are also exchanged. However, the transport of momentum by the pressure force process does not result in exchange of air; therefore, the transport of water vapor is less efficient than momentum transport.

# III. ESTIMATION OF POTENTIAL EVAPOTRANSPIRATION RATES

## A. Penman–Monteith Method

### 1. General Formulation

The energy balance at the air-surface interface in nonprecipitating conditions is usually written as

$$R_n \cong LE + H + G \tag{15}$$

where $L$ = latent heat of evaporation (J kg$^{-1}$), $E$ = water vapor flux (kg m$^{-2}$ s$^{-1}$), $H$ = sensible heat flux (W m$^{-2}$), and $G$ = soil heat flux (W m$^{-2}$), as illustrated in Figure 7. Measurements of the energy budget and application

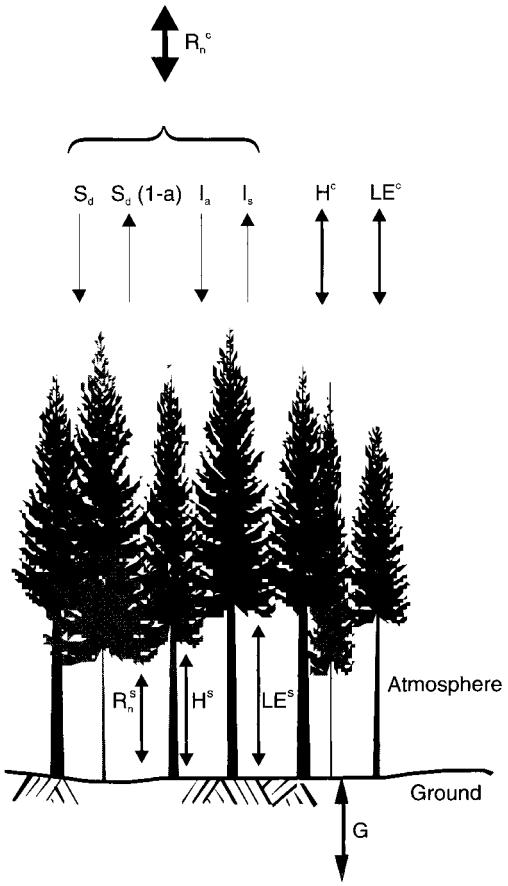


FIGURE 7 Schematic of the components of the surface energy budget.

of this formula have focused both on the interface between the top of the canopy and the free atmosphere (denoted by superscript *c*) and on the forest floor–atmosphere interface (denoted by the superscript *s*). This expression ignores photosynthesis, heat storage in plant tissue and the canopy volume, and metabolic activity, all of which tend to be smaller than the experimental error (<10% of $R_n$). Although this approximation is usually adequate and will be used in this chapter, it is important to point out that heat storage in plant tissue and the canopy volume can be significant in tall forests, particularly when net radiation is low. For example, Denmead and Bradley (1985) made estimates of this storage term for a mature Ponderosa pine (*Pinus ponderosa*) forest and found that it usually represented >10% of the net radiation, nonnegligible if high accuracy is required.

The product $LE$ is referred to as the latent heat flux. The latent heat flux is usually directed upward from the surface to the atmosphere. However, at night, condensation can occur, in which case the flow of moisture is toward the surface; however, the values of condensation are usually much lower than evaporation. Sensible heat flux ($H$) is usually directed upward into the atmosphere during the day and downward toward the canopy at night. Likewise, the soil heat flux is usually directed downward into the ground during the day and toward the surface at night. The exact partitioning of radiative energy into these components is dependent on meteorological factors, the characteristics of the soils, and the characteristics of the fuel.

The sensible and latent heat fluxes are often parameterized in terms of the near-surface gradients of temperature and vapor pressure as follows (Bonan, 1996):

$$H = \rho c_p(\theta_s - \theta_a)/r_a \tag{16}$$

and

$$LE = \frac{\rho c_p[es_s - e]}{\gamma(r_a + r_s)} \tag{17}$$

where $\theta_a$ = air potential temperature, $\theta_s$ = potential temperature of surface, $es_s$ = saturation water vapor pressure at the surface, $\gamma = c_p P/(0.622L)$, $\rho$ = air density (kg m$^{-3}$), $c_p$ = heat capacity of air at constant pressure (J kg$^{-1}$ K$^{-1}$), $r_a$ = aerodynamic resistance (s m$^{-1}$), $r_s$ = stomatal or surface resistance (s m$^{-1}$), and $P$ = pressure (hPa). $T_a$ and $e$ are measured at some standard height. For the practical problem of estimating fluxes, these formulae are difficult to apply because $T_s$ and $es_s$ are not easily measured and thus not typically available to make such estimates. Thus, many methods have been developed to estimate fluxes from more readily available measurements. In particular, numerous formulae have been developed to estimate "potential" evapotranspiration (PET) rates (i.e., that which would occur if soil water were not limited and meteorological factors only limit the rate of ET). One of the most successful and widely used of these is the Penman formula (Penman, 1948):

$$\text{PET} = \frac{\Delta(R_n - G) - \rho c_p(es - e)/r_a}{\Delta + \gamma} \tag{18}$$

This equation was modified slightly by Monteith (1965, 1981) to produce the following formula for actual evapotranspiration (AET):

$$\text{AET} = \frac{\Delta(R_n - G) + \rho c_p(es - e)/r_a}{\Delta + \gamma(1 + r_s/r_a)} \tag{19}$$

where $\Delta = d(es)/dT$ (hPa K$^{-1}$). These formulae are quite accurate for a wide range of meteorological conditions because they incorporate all the primary

meteorological factors and are based on fundamental energy conservation principles. The first term in the numerator, called the radiation term, accounts for the direct absorption of radiative energy at the air–surface interface. The second term in the numerator, the advection term, accounts for additional evaporation due to ventilation of the surface (the variable $r_a$ incorporates the wind speed; see the discussion that follows). This ventilation rate is primarily a function of the water vapor pressure deficit of the free atmosphere and the rate of turbulent mixing, which is embodied in the variable $r_a$. It is important to note that the water vapor pressure deficit used in Eqs. (18) and (19) is that at a standard measurement height, not at the air–surface interface. These often are quite different.

## 2. Aerodynamic Resistance

The rate of vertical diffusion of water vapor between the surface and the free atmosphere is parameterized by $r_s$ and $r_a$, using an analogy to electrical circuits in Ohm's law (Chapter 4 in this book) where the evaporation rate (current) is determined by the water vapor pressure deficit (voltage difference) divided by the inverse of the diffusion rate (resistance). The aerodynamic resistance ($r_a$) is inversely proportional to the rate of vertical mixing of air near the surface. In general, it is a function of the wind speed, the roughness of the surface, and the thermal stability of the near-surface atmosphere. The vertical profiles of temperature and water vapor content follow a logarithmic dependence similar to Eq. (12); $r_a$ can be derived from these logarithmic forms and expressed as

$$r_a(z) = \frac{1}{k^2 U(z)}[\ln\{(z - d)/z_0\} - \psi_m][\ln\{(z - d)/z_0\} - \psi_{m,h,w}] \qquad (20)$$

where $\psi_{m,h,w}$ is the stability correction for wind ($m$), temperature ($h$), or water vapor ($w$), depending on whether $r_a$ is used to estimate momentum, sensible heat, or latent heat fluxes, respectively. This expression for $r_a$ is based on a fundamental understanding of the nature of the turbulent near-surface atmosphere, an understanding that is supported by numerous field experiments.

Strictly speaking, the general form for $r_a$ [Eq. (20)] is applicable to fluxes of water vapor, heat, and momentum. However, as noted earlier, the efficiency of water vapor and heat transport is less than that of momentum near the surface because the pressure force does not act to transport water vapor and heat. In essence, the resistance for water vapor and heat transport is larger than for momentum transport. This is sometimes referred to as the "excess" resistance. Experimental evidence indicates that the efficiency of water vapor transport is similar to that of heat transport and these are usually assumed to be equal. Experimental observations (Chamberlain, 1968; Garratt and Hicks, 1973) have shown that the magnitude of this excess resistance is dependent on the flexibil-

ity of surface elements. Surface elements that are rigid, such as fallen logs, tree trunks, etc., are efficient at exchanging momentum by the pressure force, and, in this case, the difference between the efficiency of momentum and water vapor/heat transport is large. By contrast, flexible surface elements, such as the leaves of trees and grasses, are not very efficient at transporting momentum through the pressure force because they bend in the wind. In this case, the efficiencies for momentum and water vapor/heat transport are more nearly equivalent. A variety of expressions have been developed to parameterize this effect. Perhaps the most common and simplest approach is to assign a roughness length for water vapor and heat transport that is smaller than that for momentum. The values of $z_0$ given previously are for momentum. For water vapor or heat, a typical value is $z_{0w} = z_0/7$, where $z_{0w}$ is the roughness height for water vapor or heat (Rowntree, 1991; Shuttleworth, 1991). However, experimental evidence suggests that $z_{0w}$ is not a constant for a particular surface and, in fact, varies with environmental conditions (Blyth and Dolman, 1995; Hignett, 1994; Sun and Mahrt, 1995). Based on work by Zilitinkevich (1970), the relationship of $z_{0w}$ to $z_0$ can be expressed as

$$\ln\frac{z_0}{z_{0w}} = 0.13\left(\frac{u_* z_0}{\nu}\right)^{0.45} \tag{21}$$

where $\nu$ = kinematic viscosity of air with a value of about $1.5 \times 10^{-5}$ m$^2$ s$^{-1}$. The quantity $(u_* z_0/\nu)$ is the roughness Reynolds number, which can be interpreted as the Reynolds number of the smallest turbulent eddy. In this relationship, the ratio of $z_0$ to $z_{0w}$ increases with increasing roughness and with increasing wind speed (through $u_*$).

The excess resistance can be incorporated in Eq. (20) as follows:

$$r_a(z) = \frac{1}{k^2 U(z)}[\ln\{(z-d)/z_0\} - \psi_m][\ln\{(z-d)/z_{0w}\} - \psi_{h,w}] \tag{22}$$

A number of expressions have been derived for $\psi_m$ and $\psi_{h,w}$, based on field experiments. These are often expressed as a function of a parameter known as the Monin-Obukhov length ($L_{mo}$), defined as

$$L_{mo} = -\frac{u_*^3 \rho c_p T}{kgH} \tag{23}$$

where $L_{mo}$ has the units of length and is similar to the gradient Richardson number (Ri) in expressing the relative magnitude of wind shear forces to buoyancy forces. When the absolute magnitude of sensible heat flux ($H$) is large compared to the momentum flux, the absolute value of $L_{mo}$ is small, and vice versa. The sign of $L_{mo}$ is indicative of the stability (negative for unstable conditions, positive for stable conditions). Commonly used expressions for the wind ($\psi_m$)

and temperature/water vapor ($\psi_{h,w}$) profile correction factors are (Paulson, 1970)

$$\psi_m[(z - d)/L_{mo}] = \ln\left[\left(\frac{1 + x^2}{2}\right)\left(\frac{1 + x}{2}\right)^2\right] - 2\tan^{-1}x + \frac{\pi}{2} \qquad \text{for } L_{mo} < 0 \tag{24}$$

$$\psi_m[(z - d)/L_{mo}] = -5\frac{(z - d)}{L_{mo}} \qquad \text{for } L_{mo} > 0 \tag{25}$$

where $x = [1 - 16(z - d)/L_{mo}]^{0.25}$ and

$$\psi_{h,w}[(z - d)/L_{mo}] = 2\ln\left[\frac{1}{2}\{1 + (1 - 16(z - d)/L_{mo})^{0.5}\}\right] \qquad \text{for } L_{mo} < 0 \tag{26}$$

$$\psi_{h,w}[(z - d)/L_{mo}] = -5(d - z)/L_{mo} \qquad \text{for } L_{mo} > 0 \tag{27}$$

### 3. Stomatal or Surface Resistance

The variable $r_s$ is the resistance of the surface to the transport of water vapor. When $r_s > 0$, the surface limits ET below that of the potential rate. For dead fuels, this can be interpreted as inversely proportional to the rate of diffusion of water to the surface of the fuel. When the diffusion rate is low, it is this factor that controls ET rates, rather than the availability of energy and the rate of turbulent mixing. For leaves, $r_s$ is the stomatal resistance. The stomatal resistance reflects the physiological control on transpiration by the opening and closing of stomates in the leaf which is part of the process of photosynthesis. A number of meteorological factors influence the magnitude of $r_s$ including solar radiation, soil moisture, water vapor pressure deficit, and temperature. Because it is dependent on solar radiation, $r_s$ exhibits a pronounced and characteristic diurnal dependence as stomates open and close in response to increases and decreases in solar radiation. Stomates also respond to deficient soil moisture by partially closing to conserve water. When soil moisture is not limiting, minimum values of $r_s$ are achieved in the middle of the day and are a function of the plant type. Crops such as corn, soybean, and wheat typically have minimum values around 50 s $m^{-1}$, whereas forests have higher minimum values, typically around 100 s $m^{-1}$ or greater (Rowntree, 1991).

Some recent experiments have provided a number of observations of $r_s$ applicable to forests. Blanken *et al.* (1997) found that daytime mean values of stomatal resistance over an aspen forest varied widely, from about 50 to >200 s $m^{-1}$, with a typical daytime mean value of around 100 s $m^{-1}$. Chang *et al.* (1997) measured stomatal resistance values of 100–150 s $m^{-1}$ over a poplar

(*Populus trichocarpa* X *P. tacamahaca*) forest. Baldocchi *et al.* (1997) measured stomatal resistance over a boreal jack pine forest in Saskatchewan, Canada, and found rather high values, generally in excess of 200 s $m^{-1}$ and often exceeding 500 s $m^{-1}$. They also obtained measurements over a well-watered deciduous forest. Values of stomatal resistance were in the range of 150–400 s $m^{-1}$, somewhat lower than the jack pine forest. They argued that the high values of stomatal resistance in the jack pine forest reflect an adaptation of the plant to an environment of relatively low water availability and limits on decomposition and nutrient cycling in the boreal region where the jack pine measurements were taken. There is also experimental evidence that stomatal resistance increases when the above-canopy vapor pressure deficit exceeds approximately 10 hPa; above this threshold, stomatal resistance varies in such a way that transpiration remains relatively constant. This has been observed over an aspen forest (Hogg *et al.*, 1997), in tropical rainforests (Meinzer *et al.*, 1993; Granier *et al.*, 1996), in temperate forests and woodlands (Lopushinsky, 1986; Price and Black, 1989; Goulden and Field, 1995), and in a Holm-oak savanna (Infante *et al.*, 1997). This may reflect a physiological response of the plant to maintain leaf water potentials above the point where plant damage would occur (Tyree and Sperry, 1988; Sperry and Pockman, 1993; Goulden and Field, 1995; Goulden *et al.*, 1997).

## 4. Application of Penman–Monteith Formulae

The practical application of Eqs. (18) and (19) to estimate PET and AET is sometimes difficult because the required meteorological variables are often not available. For example, the routine hourly observations taken by National Meteorological Services at airports do not include any components of the radiation budget. By contrast, a number of specialized networks that have been established by universities, state agencies, and other organizations do include measurements of downward solar radiation and soil heat flux. However, even many of these networks do not measure net radiation.

For this reason, practical application of Eq. (17) often requires estimation of radiation components. Meyers and Dale (1983) developed a method to estimate downward solar radiation from the cloud cover observations that are taken at airports. Petersen *et al.* (1995) applied this method to develop an historical solar radiation climatology for the midwestern United States. The following methods can be used to estimate $R_n$ if hourly solar radiation observations are available or if hourly cloud observations are available to estimate solar radiation using the method of Meyers and Dale (1983) and Petersen *et al.* (1995).

A variety of investigators have found that simple regressions between $R_n$ and $S_d$ provide reasonably accurate estimates of $R_n$ with $r^2$ values greater than 0.9 (Shaw, 1956; Monteith and Szeicz, 1961; Fritschen, 1967; Nielsen *et al.*, 1981; Zhong *et al.*, 1990; Pinker and Corio, 1984; Pinker *et al.*, 1985; Kustas *et al.*,

1994; Kaminsky and Dubayah, 1997). However, these studies have produced widely varying regression coefficients. This suggests that the exact relationship between $R_n$ and $S_d$ may be rather stable for a particular location but will vary from location to location depending on other factors, probably including the latitude, temperature and humidity climatology, and land-use. Even at a specific location, the relationship will likely vary with season. Use of this approach is problematic because it may be uncertain which study's regression coefficients should be adopted.

A second method avoids some of these uncertainties by making independent estimates of the longwave components of the radiation budget. In this method, the net radiation $R_n$ is calculated following Weiss (1983) by

$$R_n = S_d(1 - a) + F_c(I_a - I_s) \tag{28}$$

where $F_c$ is a function of cloud cover. $I_a$ is given by Brutsaert (1975) as

$$I_a = 1.24(e/T_a)^{0.143}(\sigma T_a^4) \tag{29}$$

where the units are hPa ($e$) and K ($T_a$). $I_s$ is estimated by

$$I_s = 0.98\sigma T_a^4 + (1 - 0.98)I_a \tag{30}$$

$F_c$ is given by

$$F_c = 0.4 + 0.6\, C_T \tag{31}$$

where $C_T$ = cloud transmission. Soil heat flux $G$ is estimated as

$$G = 0.15\, R_n \tag{32}$$

This method is probably more accurate than the use of linear regressions between $S_d$ and $R_n$ but does require additional data (water vapor pressure, temperature, cloud cover). Cloud cover data may not be readily available for non-National Weather Service sites. Also, both $I_s$ and $I_a$ are estimated using air temperature at a standard height even though infrared emissions are determined by the surface temperature (for $I_s$) and the air temperature above the site (for $I_a$). This further reduces the accuracy.

Another approach to the estimation of PET and AET using the Penman method has been developed by Doorenbos and Pruitt (1977). This publication provides convenient tables and procedures, particularly for estimating the radiation term.

## B. Radiation Models

Empirical studies have indicated that the left- and right-hand terms of the numerator in Eqs. (18) and (19) are correlated. There is a physical basis for this finding since increasing radiation (left-hand side) will tend to increase the tem-

perature and thus the atmospheric water vapor pressure deficit (right-hand side). In humid climates, the left-hand term is typically much larger than the right-hand term. This has led to a class of models to estimate PET from radiation. Representative of this class is the Priestly–Taylor (1972) equation

$$PET = \alpha \frac{\Delta(R_n - G)}{\Delta + \gamma} \tag{33}$$

where $\alpha$ is an empirical constant to which they assigned a value of 1.26, based on analysis of field data. Other studies have been performed to estimate $\alpha$, and most of them have found values near to that of Priestly and Taylor (1972) for situations where stomatal resistance is low. However, values of $\alpha$ are often somewhat lower for forests because of higher values of stomatal resistance. For example, Blanken *et al.* (1997) measured a value of 1.22 over a hazelnut understory in an aspen forest. However, the average value of $\alpha$ above the forest canopy was only 0.91 with an upper limiting value of 1.11, indicating that stomatal control of forest transpiration substantially reduced actual evaporation below the potential value that would be calculated using a standard value of $\alpha = 1.26$.

Although application of this model requires measurements of radiation, it does not require measurements of humidity which is difficult to measure with high accuracy. This is the main attraction of this class of models. It also does not require estimates of the aerodynamic resistance and the associated uncertainties in estimating surface parameters such as $z_0$ and $d$.

## C. Pan Evaporation

Pan evaporation is measured at scattered stations around the world and provides a relatively straightforward approach to the estimation of PET. Its primary attraction is that it is a direct measure of evaporation and integrates the effects of all the meteorological controlling factors. The standard Class A pan is 121 cm in diameter and 25.5 cm deep. Data are obtained by measuring the depth of water in the pan and subtracting from the previous day's depth. Periodically, water is added to the pan. This is a simple and straightforward measurement. However, pan evaporation data must be used with care because, in general, they provide an overestimate of water loss from vegetated surfaces due primarily to two factors. First, the water volume and the pan itself absorb a greater fraction of incoming solar radiation (has a lower albedo) than vegetation. This raises the temperature of the water above the ambient air temperature and causes excessive rates of evaporation. Second, the Class A pan is raised slightly above the land surface which enhances the turbulent transport of water vapor from the

water surface to the atmosphere. These factors cause pan evaporation to be typically 20–40% higher than PET.

Correction factors, called pan coefficients, have been developed for the United States by Farnsworth and Thompson (1982) and Farnsworth *et al.* (1982). When applied to the pan evaporation data, these factors provide reasonably accurate estimates of PET. For the United States, these factors are typically in the range of 0.65–0.8, the lowest values applying to the sunny regions of the southwest and the highest values to the northern Great Lakes and west coast. Doorenbos and Pruitt (1977) also provide procedures to estimate pan coefficients, given the general climatic regime of an area and the location of the pan.

## D. Temperature Models

There is a correlation between temperature and radiation and also between temperature and water vapor pressure deficit. This has been the underlying foundation for development of models that require only temperature. One such model is the Blaney and Criddle (1950) equation which provides monthly values of PET in mm:

$$\text{PET} = C_u D(0.46\, T_m + 8) \tag{34}$$

where $C_u$ = an empirically determined consumptive use coefficient, $D$ = monthly mean percentage of annual daytime hours of the year, and $T_m$ = mean monthly temperature in °C. Values of $C_u$ have been determined for irrigated crops and typically range from 0.6 to 0.9. This method has been applied widely for irrigation applications in the western United States.

Thornthwaite (1948) developed a measure of PET that was used to classify climatic regimes, defined as

$$\text{PET}_m = 1.6\left[\frac{10\, T_m}{s}\right]^a \tag{35}$$

where

$$s = \sum_{m=1}^{12} (T_m/5)^{1.514} \tag{36}$$

and

$$a = 6.75 \times 10^{-7}\, s^3 - 7.71 \times 10^{-5}\, s^2 + 1.79 \times 10^{-2}\, s + 0.49 \tag{37}$$

where $\text{PET}_m$ is the value of PET in cm for month $m$ and $T_m$ is the mean temperature (°C) for month $m$. This formula is reasonably accurate in the humid eastern United States but underestimates PET in arid regions.

The exact relationship between PET and temperature depends on general climatic conditions, particularly arid vs. humid climates, and any temperature model must be tailored to these conditions to minimize uncertainties and errors. Even with care, such models will likely produce estimates with significant errors when meteorological conditions are climatically unusual for a location. The real attraction of such models is that temperature data are widely available. However, their use is justifiable only when data are limited to temperature and when accuracy requirements are not high.

## IV. FUNCTIONAL DEPENDENCE OF PET AND AET

The Penman-Monteith equation is used here to illustrate the dependence of PET and AET on selected meteorological variables. Figure 8 illustrates the dependence on temperature for selected values of dewpoint temperature and selected nominal values for $R_n$, $U$, $P$, and $r_s$. AET increases rather rapidly with temperature, primarily reflecting the increase in $es$ with temperature. However, there is also a contribution from the partitioning of net radiative energy between sensible and latent forms of energy. As temperature increases, an increasing fraction of net radiation is partitioned into latent heat energy. AET decreases with increasing $T_d$, reflecting decreases in the saturation vapor pressure deficit.

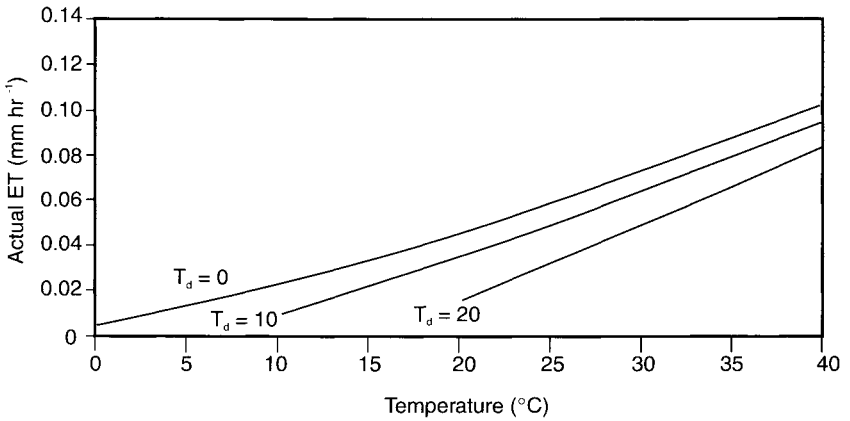


FIGURE 8 The dependence of the actual evapotranspiration on temperature for values of dewpoint temperature of 0°C, 10°C, and 20°C. Nominal values of $R_n$ = 400 W m$^{-2}$, $U$ = 5 m s$^{-1}$, $P$ = 1000 hPa, and $r_s$ = 100 s m$^{-1}$ were used to make these calculations with Eq. (19).

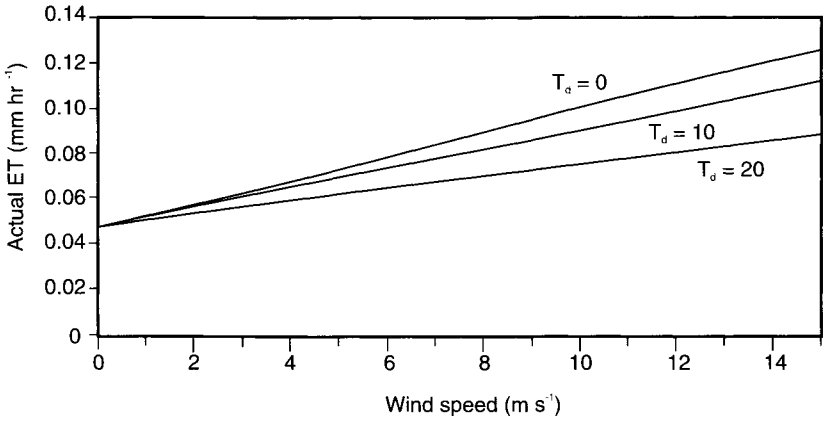


**FIGURE 9** The dependence of the actual evapotranspiration on wind speed for values of dewpoint temperature of 0°C, 10°C, and 20°C. Nominal values of $R_n$ = 400 W m$^{-2}$, $T$ = 30°C, $P$ = 1000 hPa, and $r_s$ = 100 s m$^{-1}$ were selected for these calculations using Eq. (19).

Figure 9 illustrates the dependence on wind speed for selected values of $T_d$ and nominal values for $R_n$, $T$, $P$, and $r_s$. There is a linear dependence on wind speed. The sensitivity to wind speed increases with decreasing $T_d$ (increasing water vapor pressure deficit). For these nominal values, the radiation term alone is about 0.047 mm hr$^{-1}$ ($y$ intercept). The advection term can be comparable to, or even exceed, the radiation term for moderate wind speeds and low values of $T_d$.

The dependence of AET and PET on temperature for selected values of $r_s$ is illustrated in Figure 10. The curve for $r_s$ = 0 indicates PET. As $r_s$ increases, AET decreases below PET. At higher values of $r_s$, the rate of change in AET with increasing temperature is rather small. This illustrates that, as the surface resistance increases, AET rates become less dependent on atmospheric forcing and more dependent on the characteristics of the fuel that determine the surface resistance.

Figures 8–10 illustrate that AET is a sensitive function of temperature, atmospheric water vapor content, wind speed, and stomatal or surface resistance. The use of the Penman-Monteith equation [Eq. (19)], which incorporates all of these variables, provides a suitable framework for accurate estimation of AET. By contrast, simpler approaches, such as the radiation or temperature models, do not incorporate all these variables and may result in large errors under certain conditions.

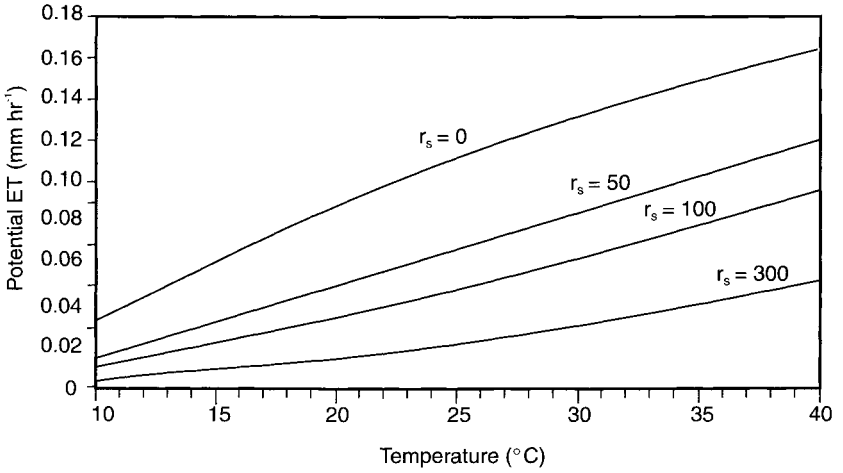


FIGURE 10 The dependence of actual evapotranspiration on temperature for values of $r_s$ = 0, 50 s m$^{-1}$, 100 s m$^{-1}$, and 300 s m$^{-1}$. Nominal values of $R_n$ = 400 W m$^{-2}$, $T_d$ = 10°C, $U$ = 5 m s$^{-1}$, and $P$ = 1000 hPa were selected for these calculations using Eq. (19). The curve for $r_s$ = 0 is the potential evapotranspiration.

## V. CHARACTERISTICS OF PET

The drying of forest fuels is related to the relative magnitudes of AET and of the amount and frequency of precipitation events. Long-term measurements of AET are not widely available. However, AET is approximately equal to PET when soil moisture levels are high. Even under deficient soil moisture levels, AET usually varies proportionally with PET. Therefore, an analysis of PET, which can be estimated from the standard meteorological observations available at many locations, provides insight into factors that affect forest fire risk.

### A. Seasonal Cycle

The seasonal variation of PET is a key factor in determining the risk of forest fires. Of particular importance is the relative magnitude of PET compared to precipitation. When PET exceeds precipitation, soil moisture can be depleted, and both live and dead fuels can lose moisture content, increasing the risk of fires. Figure 11 shows the seasonal cycle of PET at International Falls, Minnesota, based on the Penman-Monteith formula using the methodology described earlier to estimate $R_n$. The climate at this location can be classified as humid.

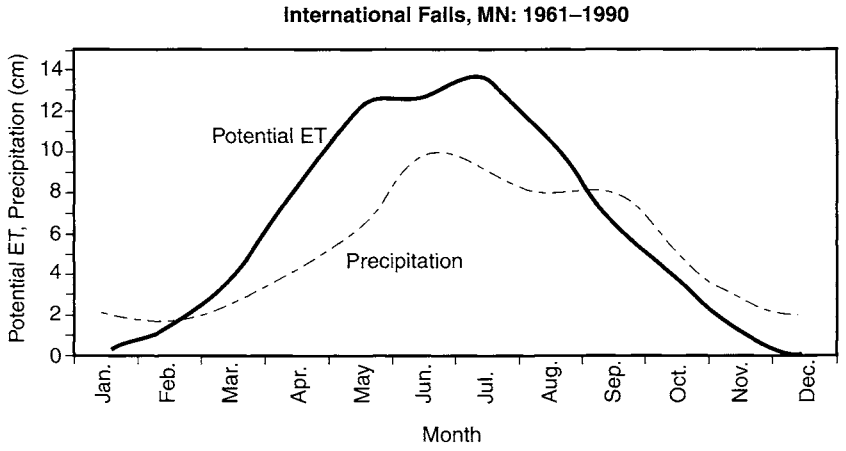


FIGURE 11 Annual cycle of average monthly potential evapotranspiration (solid) and total precipitation (dashed) for International Falls, Minnesota, based on 1961–1990 data.

Values of PET are quite low during the colder half of the year, rising rapidly during the spring and reaching a peak in mid summer. Precipitation exceeds PET during much of the colder half of the year, but during the late spring and summer months PET exceeds precipitation, on average. As a result, there is normally a depletion of soil moisture during the summer months. Often, the highest fire danger occurs in mid to late summer in this area, when soil moisture has reached its climatological minimum. The drying of dead fuels is not as sensitive to total precipitation as it is to the number of days with precipitation. This variable remains high through the summer months with about one day in three receiving some precipitation.

Variations in climatic conditions from year to year can be significant. Figure 12 shows monthly PET and precipitation at International Falls during 1980. During a very dry spring, PET exceeded precipitation substantially, resulting in early depletion of soil moisture. This can enhance the danger of spring fires before vegetation has broken dormancy when it is more flammable.

## B. Elevation Dependence

In mountainous regions, PET decreases with increasing elevation, primarily because of the dependance of temperature on elevation. During summer, temperature decreases on average by about 6°C $km^{-1}$ in much of the western United States and Canada. Even though actual water vapor pressure also decreases with height, the saturation vapor pressure usually decreases more rapidly, leading

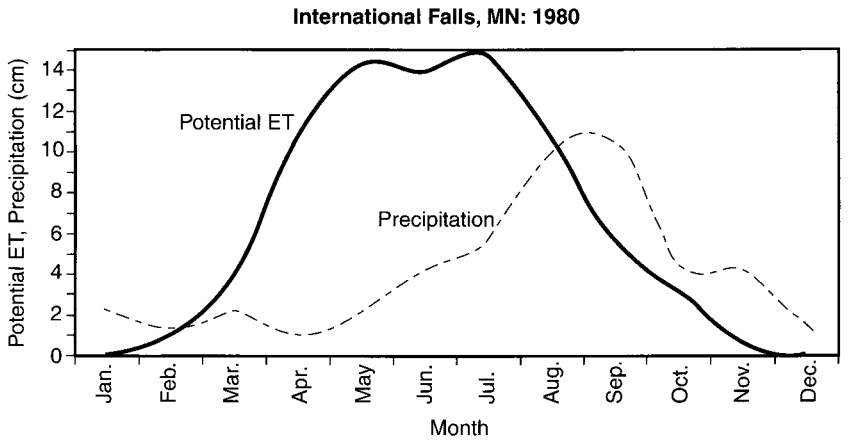


FIGURE 12 Monthly potential evapotranspiration (solid) and total precipitation (dashed) for International Falls, Minnesota, during 1980.

to a decrease in water vapor pressure deficit with increasing height. In addition, mountainous areas usually experience more cloudiness, reducing the net radiation.

An example is shown in Figure 13, which compares PET (estimated from pan evaporation data) at Flagstaff, Arizona (el. 2110 m) and Phoenix, Arizona

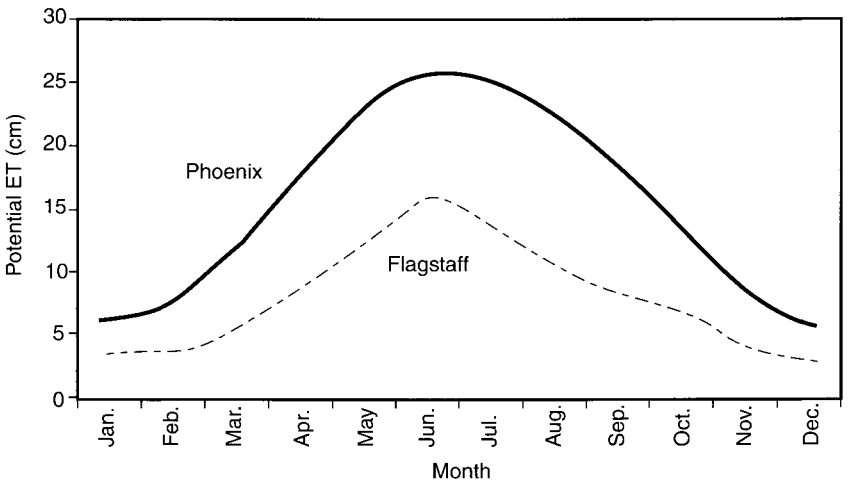


FIGURE 13 Annual cycle of monthly average potential evapotranspiration (cm) for Flagstaff, Arizona (light) and Phoenix, Arizona (dark).

(el. 323 m). The differences are due to both lower temperatures and more cloudiness at Flagstaff compared to Phoenix.

## C. Topographic Effects

Topographical effects can cause significant local variations in the surface energy budget, specifically incoming solar radiation. South-facing slopes will receive substantially greater amounts than north-facing slopes. These differences are dependent on the latitude and the time of year. Oke (1978) presents estimates of direct-beam solar radiation for a latitude of 40° at the time of the equinoxes and the solstices. He shows that differences between south-facing and north-facing slopes are smallest at the time of the summer solstice and largest at the winter solstice. Figure 14 shows an estimate of the ratio of solar radiation on a 30° south-facing slope to the radiation on a horizontal surface as a function of time of year at a latitude of 40°N, based on Jordan and Liu (1977). The ratio is highest at the winter solstice and is greater than 1 through most of the year. However, the ratio is actually less than 1 around the time of the summer solstice, indicating that a horizontal surface receives slightly more solar radiation than a 30° south-facing slope.

Measurements by Aisenshtat (1966) in the Turkestan Mountains (41°N) during September also illustrate the effect of slope. In this case, $R_n$ was nearly three times as great on a 33° south-facing slope as a 31° north-facing slope. Evapotransporation was nearly twice as large on the south-facing slope.

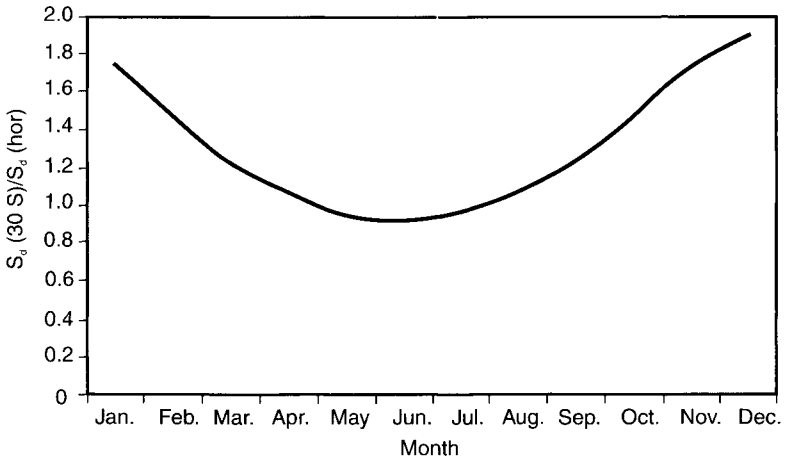


FIGURE 14 Annual cycle of the ratio of monthly average solar radiation on a 30° south-facing surface to solar radiation on a horizontal surface at a latitude of 40°N.

It is obvious that slope can have a large effect on fuel moisture content and fire risk. Fuels on south-facing slopes will, in general, tend to have lower moisture contents than those on north-facing slopes.

## D. Understory ET

Within a forest canopy, both radiation and ventilation are reduced by canopy shielding, as described earlier. Observations indicate that the magnitude of understory ET varies widely depending on the density of the understory, the type of understory vegetation, and soil moisture. Black and Kelliher (1989) reviewed field experiments and found that the ratio of understory ET to total ET varied from $<0.05$ to $>0.50$. Denmead and Bradley (1985) obtained measurements in a 16-m-high mature Ponderosa pine forest and found that understory ET was $<20\%$ of total ET. Furthermore, they found that much of the understory ET occurred from intermittent gusts of wind that ventilated the canopy. Baldocchi and Meyers (1991) measured ET at the floor of a deciduous forest and reported on the average diurnal dependence during spring and fall. Their daily average values peaked at about 25 W $m^{-2}$, or only about 0.04 mm $hr^{-1}$. Black and Kelliher (1989) reported that the ratio of understory to total ET often increases as soil moisture decreases, perhaps reflecting increases in stomatal resistance of the overstory trees as soil moisture decreases.

## VI. NEAR-SURFACE ENVIRONMENT

Chapter 4 in this book describes the relationship of the moisture content of dead fuels to relative humidity and temperature. As illustrated in Figures 4–13, the equilibrium moisture content is strongly dependent on the environmental conditions experienced by the fuel. Routine meteorological observations are taken at standard heights. For example, in the United States the standard height for measurements of maximum and minimum temperature in the National Weather Services's Cooperative Observer Network is 1.5 m. However, the actual meteorological conditions at the fuel surface are often quite different because large vertical gradients are a common feature of the near-surface atmosphere, due to the momentum, heat, and water vapor exchange that occurs at the air–surface interface. These gradients can be particularly large for ground-based fuels. A critical factor in determining the magnitude of the vertical gradients is the nature of diffusion and mixing. Within the laminar sublayer, the mixing rates are determined by molecular diffusion. Because this is quite slow, the vertical gradients are largest in this laminar sublayer. Above the laminar sublayer, mixing rates increase rapidly because the atmosphere is turbulent. Immediately above

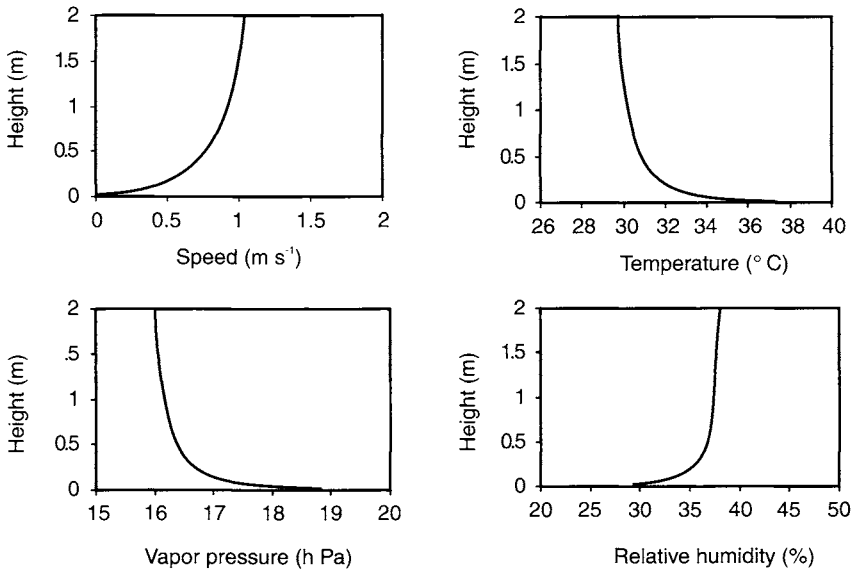


FIGURE 15 Vertical profiles of wind, temperature, water vapor pressure, and relative humidity for $H = 300$ W m$^{-2}$ and $LE = 150$ W m$^{-2}$.

the laminar sublayer, the size of turbulent eddies is restricted by proximity to the surface. The dominant size of eddies becomes larger as the distance from the surface increases. Thus, turbulent mixing rates tend to increase with height. As a consequence, the vertical gradients gradually decrease with height.

Above the laminar sublayer, the logarithmic profile that applies to the height dependence of wind speed is also observed for temperature and water vapor content. The exact dependence is a function of the magnitude of the fluxes of heat, momentum, and water vapor, as well as the characteristics of the surface, particularly the roughness height. Figure 15 shows the vertical profiles of temperature, humidity, and wind for typical mid-summer conditions over a surface that is not shielded by a forest canopy. These profiles have been calculated using empirically determined formulae that include the effects of stability (Panofsky and Dutton, 1984). As can be seen, the vertical gradients are large near the surface, gradually decreasing as height increases. Although both temperature and water vapor content increase as the surface is approached, the net effect is a decrease in relative humidity because of the exponential dependence of saturation water vapor pressure on temperature.

Figure 15 does not show what happens across the laminar sublayer. For temperature, observational evidence shows that the gradients can be very large. This is not surprising since exchange of heat occurs through molecular diffusion. Figure 16 shows an example of the diurnal dependence of the temperatures of

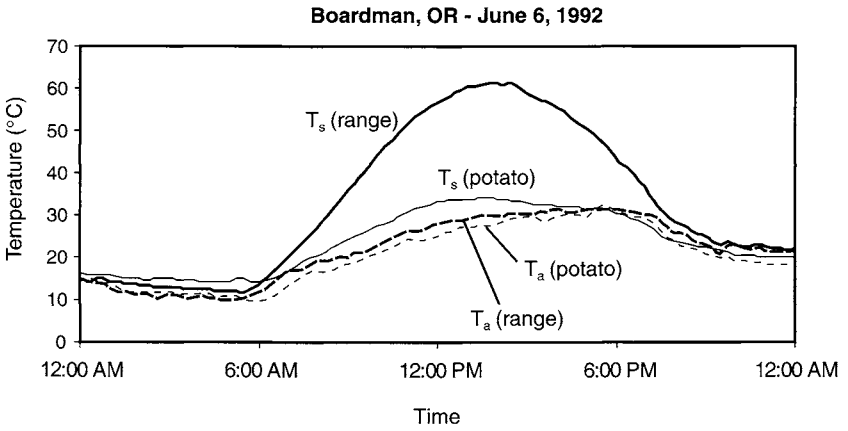


FIGURE 16 Temperature (°C) of the ground surface and the atmosphere at a height of 2 m on June 6, 1992, for a semiarid grassland (dark) and for a potato field (light) in eastern Oregon.

the surface and of the atmosphere at a height of 2 m for a semiarid grass rangeland. The temperature difference peaks at solar noon with values in excess of 30°C. This is probably typical of ground fuels. Figure 16 also shows the temperature difference for a nearby irrigated potato field. By contrast with the dry rangeland, the temperature difference over the potato field never exceeds 10°C. This contrast reflects two factors that influence this gradient. First, the rangeland is very sparsely vegetated, and momentum transport occurs largely by interactions with the solid, nonflexible ground surface rather than with the sparse grass. In the potato field, the atmospheric interactions are primarily with the flexible plants. Thus, the "excess" resistance to heat transport is higher for the rangeland than for the potato field, supporting a larger temperature gradient. The second factor is the aridity of the surface and the partitioning of net radiation into latent and sensible heat fluxes. The rangeland was quite dry, and most of the available energy was partitioned into sensible heat flux. In the irrigated potato field, latent heat flux was higher than sensible heat flux. Thus, evaporative cooling of the surface was significant in the potato field, reducing the temperature gradient.

Following Eq. (16), the surface potential temperature can be expressed as a function of the sensible heat flux, stability, wind speed, and surface roughness length, similar to Zeng and Dickinson (1998), as

$$\theta_s = \theta(z) + \frac{Hr_a(z)}{\rho c_p} \tag{38}$$

where $r_a(z)$ takes the form of Eq. (22).

Measurement of the surface temperature is relatively straightforward using small in situ probes or infrared thermometry. However, measurement of the surface water vapor content is much more difficult and such measurements have not been reported. It seems likely that the trends indicated in Figure 15 would continue across the laminar sublayer; that is, there is likely to be a substantial decrease in relative humidity at the fuel surface corresponding to the increase in temperature shown in Figure 16. Thus, ground-based fuels that are exposed to the sun experience a considerably lower relative humidity during daytime than what would be indicated by measurements at a standard measurement height. The surface water vapor content can be expressed in a similar manner to Eq. (36) as

$$e_s = e(z) + \frac{LEr_a(z)}{\rho c_p} \tag{39}$$

## VII. MODELS OF LAND–SURFACE INTERACTIONS

The preceding sections illustrate some of the complexities involved in describing mathematically the interactions of the atmosphere with the land surface and how these interactions affect drying of fuels. A great deal of effort has been devoted within the atmospheric sciences community to the development of mathematical models and associated computer software packages that can be used to describe the temporal behavior of surface fluxes of heat, momentum, and water vapor and their dependence on meteorological conditions and land surface conditions. Some of these have been developed into community models that are available to interested researchers. A brief description of their capabilities, structure, and limitations is given here. In recent years, there has been a systematic effort to improve these models through intercomparisons among these models and comparisons with field studies (T. H. Chen *et al.*, 1997). This has led to significant model improvements.

The discussion here will focus on two models, the Biosphere-Atmosphere Transfer Scheme (BATS) (Dickinson *et al.*, 1981, 1986, 1993) and the Land Surface Model (LSM) (Bonan, 1996). Both of these are community models available through the National Center for Atmospheric Research (NCAR). Most other models share many of the features of these two models. These models are quite complex, which precludes a comprehensive description. The modeling of one of the simpler cases, bare ground, will be described. This case can be applied to the problem of modeling the environmental conditions (temperature and relative humidity) experienced by a duff layer, including the diurnal dependence of those conditions.

In the absence of snow cover, the ground surface energy budget can be written as follows by combining Eqs. (3) and (15):

$$S_d(1 - a) + I_a - I_s - H - LE - G = 0 \tag{40}$$

Several of these terms are directly or indirectly a function of the surface temperature, $T_s$. To specify the surface fluxes, a value of $T_s$ must be found that satisfies Eq. (40). The upward longwave radiation, $I_s$, is parameterized by Eq. (2). The sensible heat flux, $H$, is parameterized by Eq. (16). The expression for latent heat flux [Eq. (17)] does not explicitly contain $T_s$ but is parameterized in the BATS model as

$$LE = L\rho b[q_s(T_s) - q]/r_a \tag{41}$$

where $q_s(T_s)$ is the saturated specific humidity at the surface temperature and $b$ is a soil wetness factor which ranges from 1 when the soil is wet to 0 when it is dry. This expression for $LE$ is a function of $T_s$. To determine the ground heat flux at the surface, $G(0)$, it is necessary to solve for the heat flow in the soil. This is described next. Once this is solved, $G$ can be parameterized as follows:

$$G(0) = \frac{2K_{g1}(T_s - T_{g1})}{\Delta z_1} \tag{42}$$

where $T_1$ and $\Delta z_1$ are the temperature and thickness, respectively, of the first soil layer and $K_{g1}$ is the thermal conductivity (W m$^{-1}$ K$^{-1}$) of the first soil layer.

If $S_d$ and $I_a$ are specified (e.g., they are assumed not to be a function of $T_s$), the surface temperature can be solved using the preceding parameterizations for $I_s$, $H$, $LE$, and $G$ as functions of $T_s$. Since these forms contain higher order polynomials, exponential functions, and other complex functions, it is not possible to find an analytical solution. In the LSM (Bonan, 1996), $T_s$ is found by iteratively solving the equation

$$S_d(1 - a) + I_a - I_s - H - LE - G - \left(\frac{\partial I_s}{\partial T_s} + \frac{\partial H}{\partial T_s} + \frac{\partial LE}{\partial T_s} + \frac{\partial G}{\partial T_s}\right)\Delta T_s = 0 \tag{43}$$

where $\Delta T_s = T_s^{n+1} - T_s^n$ and the superscript $n$ indicates the iteration. The time step for solution of this equation is for the order of 1 h or less.

The soil temperature profile is determined by discretizing the soil column into multiple layers. The soil heat flux at depth $z$ is

$$G(z) = K_g(z)\frac{\delta T_g}{\delta z} \tag{44}$$

One-dimensional energy conservation requires that

$$\rho_g(z)c_g(z)\frac{\delta T_g}{\delta t} = \frac{\partial}{\partial z}\left[K_g(z)\frac{\partial T_g}{\partial z}\right] \tag{45}$$

where $\rho_g(z)$ and $c_g(z)$ are the soil density and soil heat capacity, respectively, at depth $z$. In the LSM, six layers of geometrically increasing thicknesses (10, 20, 40, 80, 160, and 320 cm) are used. Equation (45) is solved by numerical methods for $T_g$ with the boundary conditions that $G(z) = 0$ at the bottom of the soil column.

The volumetric soil water content affects the density and heat capacity of the soil and the latent heat flux, as expressed in the parameter $b$ [Eq. (41)]. Thus, accurate estimation of the surface temperature requires calculation of soil water. The soil water budget must account for the movement of water vertically and for ET and precipitation at the soil–atmosphere interface. In the LSM, the change in soil water content due to the movement of water is based on the Richards equation:

$$\frac{\partial V_s}{\partial t} = \frac{\partial}{\partial z}\left[K_H\left(\frac{\partial V_s}{\partial z}\frac{\partial \Psi_s}{\partial V_s} + 1\right)\right] \tag{46}$$

where $V_s$ is the volumetric soil water content ($mm^3\ mm^{-3}$), $K_H$ is the hydraulic conductivity ($mm\ s^{-1}$), and $\Psi_s$ is the soil matrix potential (mm). This equation is combined with the accounting for evaporation and precipitation and numerically implemented for the six-layer soil column to solve for volumetric soil water.

This system of equations [Eqs. (40)–(46)] can be used to simulate the diurnal dependence of surface temperature and humidity, given a knowledge of external meteorological forcing. It is important to specify properly key parameters such as $\rho_g(z)$, $c_g(z)$, $k_g(z)$, and $K_H(z)$, since these can be quite different for organic layers compared to mineral soils. The multilayer modeling of the soil column in LSM and many other models provides a convenient framework for modeling the commonplace situation of an organic layer overlying a mineral soil.

The modeling of the surface energy budget is much more complex when a vegetative canopy is present and will not be described in detail here. In general terms, models such as BATS and LSM break this system into four major components: the plant, the atmosphere above the canopy, the atmosphere within the canopy, and the ground surface. They then explicitly account for interactions between the vegetation and the within-canopy air volume, between the within-canopy air volume and the ground surface, and between the within-canopy air volume and the atmosphere above the canopy. Radiation exchange can occur between the atmosphere and the plants, between the atmosphere and the ground surface (through gaps in the canopy overstory), and between the plants and the

ground surface. Exchange of heat and water vapor occurs between the plants and the within-canopy air volume, between the within-canopy air volume and the ground surface, and between the within-canopy air volume and the atmosphere above the canopy. Each of the processes is parameterized, and a set of state variables for each component of the system is calculated.

In addition to the modeling of radiative and sensible fluxes, another important process that is parameterized by these models is the interception of precipitation by the canopy. This can be very important in forest canopies where the surface area of the vegetation is very large. Rain will coat the vegetation with a film of water before water will fall to the ground. This water can then evaporate and return to the atmosphere. This process typically reduces the amount of rain reaching the ground surface by 10–50%. The BATS and LSM models explicitly track the storage of water on vegetative surfaces. The maximum value of this storage is assumed to be a linear function of the stem and leaf area of the vegetative canopy.

Pressing research problems, particularly the need to accurately model future climate change, are motivating work to improve these models. The ecological researcher can benefit from these advances by applying current and future land models to simulate the environmental conditions experienced by fuels.

## VIII. REMOTE SENSING OF THE SURFACE ENERGY BUDGET

There often exists substantial spatial variability in the surface energy budget, arising from spatial variations in a number of conditions, including precipitation distribution, soil water holding characteristics, and vegetation characteristics. Thus, point measurements of the surface energy budget may be representative only of a relatively small area surrounding a measurement site. Also, comprehensive measurements of the components of the surface energy budget are taken at very few sites because of the cost and difficulty. For these reasons, there has been considerable research investigating the use of remote sensors on airborne or satellite platforms to make such measurements.

One widely used technique relies on the parameterization of $H$ expressed in Eq. (16). In this relationship, $H$ is proportional to the difference in temperature between the surface and the overlying atmosphere. Thermal infrared measurements are routinely obtained by several satellites, providing an estimate of the surface radiative temperature ($T_s$). The air temperature ($T_a$) can be estimated from the surface observing network. The aerodynamic resistance ($r_a$) must be estimated, requiring values for the roughness height and wind speed. Thus, some knowledge of the characteristics of the surface is necessary.

The latent heat flux ($LE$) is often estimated as a residual of the terms in Eq. (15). This requires an estimate of the radiative terms in Eq. (3). Values of $S_d$ and albedo can be retrieved from geostationary satellites (Tarpley, 1979; Gautier *et al.*, 1980; Diak and Gautier, 1983) using methods in which cloudiness is the major factor modulating solar radiation at the surface. The infrared radiation terms ($I_a$ and $I_s$) can be estimated from thermal radiation satellite measurements. The soil heat flux ($G$) is usually small compared to $H$ and can be estimated with sufficient accuracy using a combination of the measurement of $T_s$ and a model, such as Eq. (42).

Although the basic approach (Jackson *et al.*, 1977; Seguin and Itier, 1983) for estimating $H$ has changed little, there have been a number of variations, resulting in a rather large number of models (Olioso *et al.*, 1999; Schmugge and Becker, 1991). These models have been somewhat successful in providing large-scale estimates of $H$ and $LE$ (Lagouarde, 1991).

The accuracy of remote sensing estimates of surface fluxes using thermal IR measurements is limited by the precision of the measurement of $T_s$, which is of the order of 2–3 K. In many situations, the temperature difference ($T_s - T_a$) is of the same order of magnitude. In these situations, the estimates of the surface fluxes are not highly accurate. Typically, under the best circumstances, the sensible heat flux can be estimated to within $\pm 30$ W m$^{-2}$ (Seguin *et al.*, 1999). A complication arises when the surface is partially covered with vegetation. Often, the vegetative elements and the bare ground have very different radiative temperatures. Intercomparison of some of these models suggests that, with partial vegetative cover, separate accounting for the fluxes from the bare ground and from the vegetative elements provides superior results (Zhan *et al.*, 1996). Estimates of vegetative cover using the Normalized-Difference Vegetation Index (NDVI) can provide more accurate estimates of the components of the surface energy budget (Boegh *et al.*, 1999; Inoue and Moran, 1997).

There has also been a significant amount of work investigating the use of remote sensors to estimate surface soil moisture. One approach relies on passive microwave radiometry. The surface brightness temperature in the microwave portion of the spectrum is a highly sensitive function of volumetric soil moisture. Aircraft measurements using microwave radiometers have achieved accuracies of $\pm 3\%$ in measurement of the volumetric soil water (Jackson *et al.*, 1995). One limitation of passive microwave approaches is that satellite sensors can achieve only rather crude resolution (10–30 km). Another proposed approach utilizes active microwave sensors which can obtain multifrequency, multipolarization data at rather high spatial resolution. This approach shows promise of achieving accurate estimates of soil moisture at high resolution (Bindlish and Barros, 2000).

Despite some of the limitations and uncertainties, remote sensing of the surface energy budget holds potential as a tool to assess the variability of fuel moisture on regional scales (1–100 km).

# IX. FIRE WEATHER RATING SYSTEMS

Fire weather rating systems incorporate measures of drying that reflect the physical basis for ET described in this chapter. To illustrate this, the United States and Canadian rating systems are briefly discussed.

## A. United States

The National Fire Rating System of the United States is based in part on indices of the fuel moisture of both dead and live fuels. The relationships among environmental conditions and fuel moisture are empirically based. The drying of dead fuels under constant conditions is assumed to follow an exponential decay curve. Dead fuels are stratified into four categories of time response: 1, 10, 100, and 1000 h. A key concept in this system is the equilibrium moisture content (EMC) which is the "moisture content dead fuels would obtain if left in a steady state environment long enough to obtain equilibrium (no net moisture exchange)" (Bradshaw *et al.*, 1983). The EMC is calculated from temperature and relative humidity using regression equations developed by Simard (1968). These equations are

$$\text{EMC} = \begin{cases} 0.03299 + 0.281073\ \text{RH} - 0.00058\ \text{RH}\ T & \text{RH} < 10 \\ 2.22749 + 0.160107\ \text{RH} - 0.0148\ T & 10 < \text{RH} < 50 \\ 21.06060 + 0.005565\ \text{RH}^2 - 0.0035\ \text{RH}\ T - 0.483199\ \text{RH} & \text{RH} > 50 \end{cases} \tag{47}$$

Figure 17 shows this relationship as a function of RH for various values of temperature, indicating that the EMC is highly sensitive to RH and slightly sensitive to temperature.

An important consideration in the application of the preceding formula is that the relative humidity and temperature values are those at the surface of the dead fuel, not at the normal observational height of instruments. As noted in the previous section, these values can be quite different, particularly during sunny daytime conditions. To account for the near-surface gradient, the rating system uses adjustment factors that are applied to the observed temperature and relative humidity; these are a function of sky cover conditions and are shown in Table 1 (Bradshaw *et al.*, 1983). As this table shows, the adjustment for temperature and relative humidity are large under sunny conditions but quite consistent with observations, as illustrated in Figures 15 and 16. These adjusted factors are used in the EMC regression equations. These corrections are applied to mid-afternoon observations when relative humidity reaches its minimum value and fuel moisture content would be at a minimum.

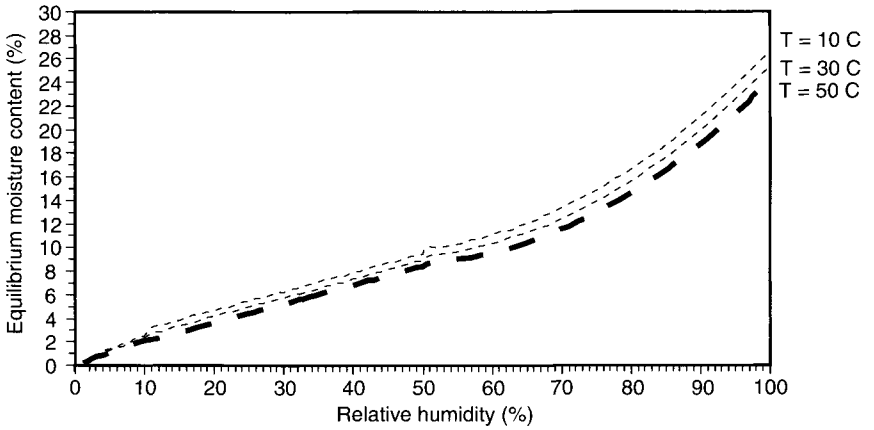


FIGURE 17 Equilibrium moisture content (%) of dead fuels as a function of relative humidity for values of temperature = 10, 30, and 50°C as calculated in the U.S. National Fire Rating System.

For 1- and 10-h fuels, mid-afternoon observations are used to estimate fuel moisture content. This reflects the substantial variation of RH within the daily cycle (Figure 5) and the need to incorporate this into the rating system for fast response fuels. To compute fuel moisture content for 100-h fuels, a weighted 24-h average EMC value is used; this is calculated from the day's maximum and minimum temperature and maximum and minimum relative humidities. For 1000-h fuels, EMC is averaged over 7-day periods.

Two types of classes are used for live fuels: grass forbs and woody shrubs. The system's developers found that the 1000-h fuel moisture function responded to meteorological conditions in a similar fashion to that expected for live fuel. The system thus applies this function to estimate live fuel moisture. Of course, plants are adapted to their environment. Those adapted to drier conditions tend to use moisture more slowly than those adapted to wetter conditions. Thus, the fire danger rating system uses parameters that are a function of climatic zone, as

TABLE 1 Temperature and Relative Humidity Adjustment Factors for Calculation of Equilibrium Moisture Content

| Fractional sky cover | Temperature adjustment (°F) | Relative humidity adjustment |
|---|---|---|
| 0.0–0.1 | +25 | × 0.75 |
| 0.1–0.5 | +19 | × 0.83 |
| 0.5–0.9 | +15 | × 0.91 |
| 0.9–1.0 | +5 | × 1.0 |

determined by the Thornthwaite climate classification scheme. In this system, there are four climate classes: arid and semiarid, subhumid, humid, and wet.

## B. Canada

The Canadian Forest Fire Weather Index System (Van Wagner, 1987) uses three separate indices for three distinct dead fuel classes:

1. Fine Fuel Moisture Code (FFMC), which represents the moisture content of litter and other fine fuels, with a time lag of less than one day.
2. Duff Moisture Code (DMC), which represents the moisture content of loosely compacted organic matter, with a time lag of 12 days.
3. Drought Code (DC), representing a deep layer of compact organic matter with a time lag of 52 days.

There are a number of basic similarities between the Canadian system and the U.S. system, although some of the functional relationships are different. In the Canadian system, an equilibrium moisture content is calculated which is a function of relative humidity and temperature. This is used in the computation of the FFMC. The functional dependence exhibits hysteresis; specifically, the equilibrium moisture content is lower during wetting than during drying. Fuel moisture content approaches the equilibrium value in an exponential manner, much as in the U.S. system. The rate of change is a function of wind speed, relatively humidity, temperature, and (in the case of the DMC and DC) the day length (which is a surrogate for radiation). Thus, all the major meteorological factors that affect ET are incorporated in an empirical manner.

The DMC uses a constant equilibrium moisture content of 20%. The rate of drying is a function of temperature, relative humidity, and an empirical day length factor. This function does not include any wind speed dependence. This is a reflection of the control on ET by surface resistance ($r_s$). When $r_s$ is large, the aerodynamic resistance, which incorporates the wind speed dependence, is relatively less important. Evaporative drying for the DC index is based on an estimate of potential evaportransporation which is calculated from an empirical function of noon time temperature and a day length factor.

## NOTATION

### Roman Letters

| | | |
|---|---|---|
| $a$ | albedo | dimensionless |
| $A, B, C$ | constants used in formula relating $es$ to $T$ | |

| | | |
|---|---|---|
| $b$ | soil wetness factor (0–1) | |
| $c_p$ | heat capacity of air at constant pressure | $m^2 s^{-2} K^{-1}$ |
| $c_g$ | heat capacity of the soil | $J kg^{-1} K^{-1}$ |
| $C_T$ | cloud radiation transmission | dimensionless |
| $C_u$ | empirically-determined consumptive use coefficient | |
| $d$ | displacement height | m |
| $D$ | monthly mean percentage of annual daytime hours of the year | % |
| $e$ | atmospheric water vapor pressure | hPa |
| $es$ | saturation value of atmospheric water vapor pressure | hPa |
| $E$ | water vapor flux | $kg m^{-2} s^{-1}$ |
| EMC | equilibrium moisture content | % |
| $ET$ | evapotranspiration | $kg m^{-2} s^{-1}$, $W m^{-2}$, or $mm h^{-1}$ |
| $F_c$ | function relating net infrared radiation to cloud cover | dimensionless |
| $G$ | soil heat flux | $W m^{-2}$ |
| $h$ | height of the vegetative canopy | m |
| $H$ | sensible heat flux | $W m^{-2}$ |
| $I$ | infrared radiation | $W m^{-2}$ |
| $k$ | von Karman constant (= 0.4) | dimensionless |
| $K_g$ | thermal conductivity of the soil | $Wm^{-1} K^{-1}$ |
| $K_H$ | soil hydraulic conductivity | $mm s^{-1}$ |
| $L$ | latent heat of evaporation | $J kg^{-1}$ |
| $L_{mo}$ | Monin-Obukhov length | m |
| $P$ | air pressure | hPa |
| $P_o$ | reference level pressure | hPa |
| $PET$ | potential evapotranspiration | $W m^{-2}$ or $mm h^{-1}$ |
| $PET_m$ | accumulated value of PET for month m | cm |
| $q$ | specific humidity | kg $H_2O$/kg moist air |

| | | |
|---|---|---|
| $r$ | resistance | $s\ m^{-1}$ |
| $R_n$ | net radiation | $W\ m^{-2}$ |
| $RH$ | relative humidity | % |
| $Ri$ | gradient Richardson number | dimensionless |
| $S_d$ | downward solar radiation at the earth's surface | $W\ m^{-2}$ |
| $T$ | temperature | °C |
| $T_d$ | dew point temperature | °C |
| $T_m$ | mean monthly temperature | °C |
| $u_*$ | friction velocity | $m\ s^{-1}$ |
| $U(z)$ | wind speed at height z | $m\ s^{-1}$ |
| $v$ | atmospheric water vapor mixing ratio | kg $H_2O$/ kg dry air |
| $vs$ | saturation water vapor mixing ratio | kg $H_2O$/ kg dry air |
| $V_s$ | volumetric soil water content | $mm^3\ mm^{-3}$ |
| $z$ | height above ground surface or depth in soil | m |
| $z_0$ | roughness length for momentum transport | m |
| $z_{ow}$ | roughness length for water vapor transport | m |

## Greek Letters

| | | |
|---|---|---|
| $\alpha$ | empirical constant used in Priestley-Taylor formula for *PET* | dimensionless |
| $\beta$ | wind velocity attenuation coefficient | |
| $\Delta$ | $des/dT$ | $hPa\ K^{-1}$ |
| $\varepsilon$ | emissivity | dimensionless |
| $\gamma$ | $c_p P/(0.622L)$ | $hPa\ K^{-1}$ |
| $\upsilon$ | kinematic viscosity of air | $m^2\ s^{-1}$ |
| $\Psi_s$ | soil matrix potential | mm |
| $\psi$ | vertical profile adjustment factor for temperature, wind, and water vapor | dimensionless |
| $\rho$ | air density | $kg\ m^{-3}$ |
| $\sigma$ | Stefan Boltzmann constant ($5.67 \times 10^{-8}\ Wm^{-2}\ K^{-4}$) | $W\ m^{-2}\ K^{-4}$ |
| $\theta$ | potential temperature | K |

## SUBSCRIPTS

| | |
|---|---|
| $a$ | air or aerodynamic |
| $g$ | soil |
| $h$ | temperature |
| $m$ | wind |
| $s$ | surface of soil or vegetative canopy |
| $w$ | water vapor |

## SUGGESTED READING LIST

Campbell, G. S., and Norman, J. M. (1998). "An Introduction to Environmental Physics." Springer-Verlag, New York.

Panofsky, H. A., and Dutton, J. A. (1984). "Atmospheric Turbulence: Models and Methods for Engineering Applications." John Wiley and Sons, New York.

Rosenberg, N. J. (1974). "Microclimate: The Biological Environment." John Wiley and Sons, New York.

Schmugge. T. J., and Andre, J.-C., Eds. (1991). "Land Surface Evaporation: Measurement and Parameterization." Springer-Verlag, New York.

## REFERENCES

Aisenshtat, B. A. (1966). Investigations of the heat budget of central Asia. *In* "Sowremennye Problemy Klimatologii" (M. I. Budyko, Ed.), pp. 83–129. Meteorol. Gidrol, Leningrad.

Baldocchi, D. O., and Meyers, T. P. (1991). Trace gas exchange at the floor of a deciduous forest: I. Evaporation and $CO_2$ efflux. *J. Geophys. Res.* **96**, 7271–7285.

Baldocchi, D. D., and Vogel, C. A. (1996). Energy and $CO_2$ flux densities above and below temperate and broad leafed forest and a boreal pine forest. *Tree Physiol.* **16**, 5–16.

Baldocchi, D. D., Vogel, C. A., and Hall, B. (1997). Seasonal variation of energy and water vapor exchange rates above and below and boreal jack pine forest canopy. *J. Geophys. Res.* **102**, 28,939–28,951.

Betts, A. K., and Ball, J. H. (1997). Albedo over the boreal forest. *J. Geophys. Res.* **102**, 28,901–28,909.

Bindlish, R., and Barros, A. P. (2000). Multifrequency soil moisture inversion from SAR measurements with the use of IEM. *Remote Sens. Environ.* **71**, 67–88.

Black, T. A., and Kelliher, F. M. (1989). Processes controlling understory evaporation. *Phil. Trans. Roy. Soc. (Lond) B.* **324**, 207–231.

Blaney, H. F., and Criddle, W. O. (1950). "Determining Water Requirements in Irrigated Data." U.S. Department of Agriculture Soil Conservation Service Technical Paper No. 96.

Blanken, P. D., Black, T. A., Yang, P. C., Neumann, H. H., Nesic, Z., Staebler, R., den Hartog, G., Novak, M. D., and Lee, X. (1997). Energy balance and canopy conductance of a boreal aspen forest: Partitioning overstory and understory components. *J. Geophys. Res.* **102**, 28,915–28,927.

Blyth, E. M., and Dolman, A. J. (1995). The roughness length for heat of sparse vegetation. *J. Appl. Meteorol.* **34**, 583–585.

Boegh, E., Soegaard, H., Hanan, N., Kabat, P., and Lesch, L. (1999). A remote sensing study of the NDVI-$T_s$ relationship and the transpiration from sparse vegetation in the Sahel based on high-resolution data. *Remote Sens. Environ.* **69**, 224–240.

Bonan, G. B. (1996). "A Land Surface Model (LSM Version 1.0) for Ecological Hydrological, and Atmospheric Studies Technical Description and User's Guide." NCAR Technical Note NCAR/TN-417+STR. National Center for Atmospheric Research, Boulder.

Bradshaw, L. S., Deeming, J. E., Burgan, R. E., and Cohen, J. D. (1983). "The 1978 National Fire Danger Rating System: Technical Documentation." General Technical Report INT-169, U.S. Department of Agriculture, Forest Service, Intermountain Forest and Range Experiment Station, Ogden.

Brown, A. A., and Davis, K. P. (1973). "Forest Fire: Control and Use." McGraw-Hill, New York.

Brutsaert, W. (1975). On a derivable formula for long-wave radiation from clear skies. *Water Resour. Res.* **11**, 742–744.

Buck, A. L. (1981). New equations for computing vapor pressure and enhancement factors. *J. Appl. Meteorol.* **20**, 1527–1532.

Chamberlain, A. C. (1968). Transport of gases to and from surfaces with bluff and wave-like roughness elements. *Quart. J. Roy. Meteorol. Soc.* **94**, 318–332.

Chandler, C., Cheney, P., Thomas, P., Trabaud, L., and Williams, D. (1983). "Fire in Forestry: Volume One. Forest Fire Behavior Effects." John Wiley and Sons, New York

Chang, H., Simmonds, L. P., Morison, J. I. L., and Payne, D. (1997). Estimation of transpiration by single trees: Comparison of sap flow measurements with a combination equation. *Agric. For. Meteorol.* **87**, 155–169.

Chen, J. M., Rich, P. M., Gower, S. T., Norman, J. M., and Plummer, S. (1997). Leaf area index of boreal forests: Theory, techniques, and measurements. *J. Geophys. Res.* **102**, 29,429–29,443.

Chen, T. H., Henderson-Sellers, A. Milly, P. C. D., Pitman, A. J., Beljaars, A. C. M., Polcher, J., Abramopoulus, F., Boone, A., Chang, S., Chen, F., Dai, Y., Desbouough, E. E., Dickinson, R. E., Dumenil, L., Ek, M., Garratt, J. R., Gedneny, N., Gusew, Y. M., Kim, J., Koster, R., Kowalczyk, E. A., Loval, K., Lean, J., Lettenmaier, D., Liang, X., Makfouf, J.-F., Mengelkamp, H.-T., Mitchell, K., Nanonova, O. N., Noilhan, J., Robock, A., Rozenzweig, C., Schaake, J., Schlosser, C. A., Schulz, J.-P., Shao, Y., Shimakin, A. B., Verseghy, D. L., Wetzel, P., Wood, E. F., Xue, Y., Yang, Z.-L., and Zeng, Q. (1997). Cabauw experimental results from the Project for Intercomparison for Land-Surface Parameterization Schemes. *J. Climate* **10**, 1194–1215.

Cionco, R. M. (1965). A mathematical model for air flow in a vegetative canopy. *J. Appl. Meteorol.* **4**, 517.

Cionco, R. M. (1978). Analysis of canopy index values for various canopy densities. *Boundary-Layer Meteorol.* **15**, 81–93.

Denmead, O. T., and Bradley, E. F. (1985). Flux-gradient relationships in a forest canopy. *In* "The Forest-Atmosphere Interaction" (B. A. Hutchison and B. B. Hicks, Eds.), pp. 543–561. D. Riedel, Dordrecht.

Diak, G., and Gautier, C. (1983). Improvements to a simple model for estimating insolation from GOES data. *J. Clim. Appl. Meteorol.* **22**, 505–508.

Dickinson, R. E., Henderson-Sellers, A., and Kennedy, P. J. (1993). "Biosphere-Atmosphere Transfer Scheme (BATS) Version 1e as Coupled to the NCAR Community Climate Model." NCAR Technical Note NCAR/TN-387+STR. National Center for Atmospheric Research, Boulder.

Dickinson, R. E., Henderson-Sellers, A., Kennedy, P. J., and Wilson, M. F. (1986). "Biosphere-Atmosphere Transfer Scheme (BATS) for the NCAR Community Climate Model." NCAR Technical Note/TN-275+STR. National Center for Atmospheric Research, Boulder.

Dickinson, R. E., Jaeger, J., Washington, W. M., and Wolske, R. (1981). "Boundary Subroutine for the NCAR Global Climate Model." NCAR Technical Note/TN-173+1A. National Center for Atmospheric Research, Boulder.

Doorenbos, J., and Pruitt, W. O. (1977). "Crop Water Requirements." F.A.O. Irrigation and Drainage Paper 24. F. A. O., Rome.

Farnsworth, R. K., and Thompson, E. S. (1982). "Mean Monthly, Seasonal, and Annual Pan Evaporation for the United States." NOAA Technical Report NWS 34. U.S. Department of Commerce, Washington, DC.

Farnsworth, R. K., Thompson, E. S., and Peck, E. L. (1982). "Evaporation Atlas for the Contiguous 48 United States." NOAA Technical Report NWS 33. U.S. Department of Commerce, Washington, DC.

Fritschen, L. J. (1967). Net and solar-radiation relations over irrigated field crops. *Agric. Meteorol.* **4**, 55–62.

Fritchen, L. J. (1985). Characterization of boundary condtions affecting forest environmental phenomena. *In* "The Forest-Atmosphere Interaction" (B.A. Hutchison and B. B. Hicks, Eds.), pp. 3–23. D. Riedel, Dordrecht.

Garratt, J. R., and Hicks, B. B. (1973). Momentum, heat and water vapour transfer to and from natural and artificial surfaces. *Quart. J. Roy. Meteorol. Soc.* **99**, 680–687.

Garratt, J. R. (1977). "Aerodynamic Roughness and Mean Monthly Surface Stress over Australia." CSIRO Aust. Div. Atmos. Phys. Tech. Paper No. 29. CSIRO, Melbourne.

Gautier, C., Diak, G., and Masse, S. (1980). A simple physical model to estimate incident solar radiation at the surface from GOES satellite data. *J. Appl. Meteorol.* **19**, 1005–1012.

Goulden, M. L., Daube, B. C., Fan, S.-M. Sutton, D. J., Bazzaz, A., Munger, J. W., and Wofsy, S. C. (1997). Physiological responses of a black spruce forest to weather. *J. Geophys. Res.* **102**, 28,987–28,996.

Goulden, M. L., and Field, C. B. (1995). Three methods for monitoring the gas exchange of individual tree canopies: Ventilated-chamber, sap-flow and Penman-Montieth measurements on evergreen oaks. *Funct. Ecol.* 8, 125–135.

Granier, A., Huc, R., and Barigah, S. T. (1996). Transpiration of natural rain forest and its dependence on climatic factors. *Agric. For. Meteorol.* **78**, 19–29.

Hignett, P. (1994). Roughness lengths for temperature and momentum over heterogeneous terrain. *Boundary Layer Meteorol.* **68**, 225–236.

Hodges, G. B., and Smith, E. A. (1997). Intercalibration, objective analysis, intercomparison and synthesis of BOREAS surface net radiation measurements. *J. Geophys. Res.* **102**, 28,885–28,900.

Hogg, E. H., Black, T. A., den Hartog, G., Neumann, H. H., Zimmermann, R., Hurdle, P., Blanken, P. D., Nesic, Z., Yang, P. C., Staebler, R. M., McDonald, K. C., and Oren, R. (1997). A comparison of sap flow and eddy fluxes of water vapor from a boreal deciduous forest. *J. Geophys. Res.* **102**, 28,929–28,937.

Infante, J. M., Rambal, S., and Joffre, R. (1997). Modeling transpiration in Holm-oak savanna: Scaling up from the leaf to the tree scale. *Agric. For. Meteorol.* **87**, 273–289.

Inoue, Y., and Moran, M. S. (1997). A simplified method for remote sensing of daily canpy transpiration—A case study with direct measurements of canopy transpiration in soybean canopies. *Int. J. Remote Sens.* **18**, 139–152.

Jackson, R. D., Reginato, R. J., and Idso, S. B. (1977). Wheat canopy temperature: A practical tool for evaluating water requirements. *Water Resour. Res.* **13**, 651–656.

Jackson, T. J., LeVine, D. M., Swift, C. T., Schmugge, T. J., and Schiebe, F. R. (1995). Large area mapping of moisture using the ESTAR passive microwave radiometer in Washita '92. *Remote Sens. Environ.* **53**, 27–37.

Jordan, R. C., and Liu, B. Y. H. (Eds.). (1977). "Applications of Solar Energy for Heating and Cooling of Buildings." American Society of Heating, Refrigerating, and Air-Conditioning Engineers, Inc., New York.

Kaminsky, K. Z., and Dubayah, R. (1997). Estimation of surface net radiation in the boreal forest and northern prairie from shortwave flux measurements. *J. Geophys. Res.* **102**, 29,707–29,716.

Kustas, W. P., Pinker, R. T., Schmugge, T. J., and Humes, K. S. (1994). Daytime net radiation estimated for a semiarid rangeland basin from remotely sensed data. *Agric. For. Meteorol.* **71**, 337–357.

Lagouarde, J.-P. (1991). Use of NOAA AVHRR date combined with an agrometeorological model for evaporation mapping. *Int. J. Remote Sens.* **12**, 1853–1864.

List, R. J. (1949). "Smithsonian Meteorological Tables," 6th ed. Smithsonian Institution Press, Washington, DC.

Lopushinsky, W. (1986). Seasonal and diurnal trends of heat pulse velocity in Douglas-fir and ponderosa pine. *Can. J. For. Res.* **16**, 814–821.

McCaughey, J. H. , Lafleur, P. M., Joiner, D. W., Bartlett, P. A., Costello, A. M., Jelinski, D. E., and Ryan, M. G. (1997). Magnitudes and seasonal patterns of energy, water, and carbon exchanges at a boreal young jack pine forest in the BOREAS northern study area. *J. Geophys. Res.* **102**, 28,997–29,007.

Meinzer, F. C., Goldstein, G., Holbrook, N. M., Jackson, P., and Cavelier, J. (1993). Stomatal and environmental control of transpiration in a lowland tropical forest tree. *Plant Cell Environ.* **16**, 429–436.

Meyers, T. P., and Dale, R. F. (1983). Predicting daily insolation with hourly cloud height and coverage. *J. Clim. Appl. Meteorol.* **22**, 537–545.

Monteith, J. L. (1965). Evaporation and the environment. *Symp. Soc. Exp. Biol.* **19**, 205–234.

Monteith, J. L. (1981). Evaporation and surface temperature. *Quart. J. Roy. Meteorol. Soc.* **107**, 1–27.

Monteith, J. L., and Szeicz, G. (1961). The radiation balance of bare soil and vegetation. *Quart. J. Roy. Meteorol. Soc.* **87**, 159–170.

Nielsen, L. B., Prahm, L. P., Berkowicz, R., and Conradsen, K. (1981). Net incoming radiation estimated from hourly global radiation and/or cloud observations. *J. Climatol.* **1**, 255–272.

Oke, T. R. (1978). "Boundary Layer Climates." Methuen, London.

Olioso, A., Chauki, H., Courault, D., and Wigneron, J.-P. (1999). Estimation of evapotranspiration and photosynthesis by assimilation of remote sensing data into SVAT models. *Remote Sens. Environ.* **68**, 341–356.

Panofsky, H. A., and Dutton, J. A. (1984). "Atmospheric Turbulence: Models and Methods for Engineering Applications." John Wiley and Sons, New York.

Paulson, C.A. (1970). The mathematical representation of wind speed and temperature profiles in the unstable atmospheric surface layer. *J. Appl. Meteorol.* **9**, 857–861.

Penman, H. L. (1948). Natural evaporation from open water, bare soil, and grass. *Proc. Roy. Soc. (Lond) A.* **193**, 120–145.

Petersen, M. S., Lamb, P. J., and Kunkel, K. E. (1995). Implementation of a semi-physical model for examining solar radiation in the Midwest. *J. Appl. Meteorol.* **34**, 1905–1915.

Pinker, R. T., and Corio, L. A. (1984). Surface radiation budget from satellites. *Mon. Wea. Rev.* **112**, 209–215.

Pinker, R. T., Corio, L. A., and Tarpley, J. D. (1985). The relationship between planetary and surface net radiation. *J. Clim. Appl. Meteorol.* **24**, 1272–1268.

Price, D. T., and Black, T. A. (1989). Estimation of forest transpiration and $CO_2$ uptake using the Penman-Montieth equation and a physiological photosynthesis model. *In* "Proceedings of Workshop on Estimation of Areal Evapotranspiration," pp. 213–228. IAHS Pub. 177, Vancouver.

Priestley, C. H. B., and Taylor, R. J. (1972). On the assessment of surface heat flux and evaporation using large scale parameters. *Mon. Wea. Rev.* **100**, 81–92.

Pyne, S. J. (1984). "Introduction to Wildland Fire: Fire Management in the United States." John Wiley and Sons, New York.

Rowntree, P. R. (1991). Atmospheric parameterization schemes for evaporation over land: Basic concepts and climate modeling aspects. *In* "Land Surface Evaporation: Measurement and Parameterization" (T. J. Schmugge and J.-C. André, Eds.), pp. 5–29. Springer-Verlag, New York.

Salby, M. L. (1996). "Fundamentals of Atmospheric Physics." Academic Press, San Diego.

Schmugge, T. J., and Becker, F. (1991). Remote sensing observations for the monitoring of land–surface fluxes and water budgets. *In* "Land Surface Evaporation: Measurement and Parameterization" (T. J. Schumgge and J.-C. Andre, Eds.), pp. 337–347. Springer-Verlag, New York.

Seguin, B., and Itier, B. (1983). Using midday surface temperature to estimate daily evaporation from satellite thermal IR data. *Int. J. Remote Sens.* **4**, 371–383.

Seguin, B., Becker, F., Phulpin, T., Gu, X. F., Guyot, G., Kerr, Y., King, C., Lagouarde, J. P., Ottle, C., Stoll, M. P., Tabbagh, A., and Vidal, A. (1999). IRSUTE: A minisatellite project for land surface heat flux estimation from field to regional scale. *Remote Sens. Environ.* **68**, 357–369.

Sellers, P. J., Hall, F. G., Kelly, R. D., Black, A., Baldocchi, D., Berry, J., Ryan, M., Ranson, K. J., Crill, P. M., Lettenmaier, D. P., Margolis, H., Cihlar, J., Newcomer, J., Fitzjarrald, D., Jarvis, P. G., Gower, S. T., Halliwell, D., Williams, D., Goodison, B., Wickland, D. E., and Guertin, F. E. (1997). BOREAS in 1997: Experiment overview, scientific results, and future directions. *J. Geophys. Res.* **102**, 28,731–28,769.

Shaw, R. H. (1956). A comparison of solar radiation and net radiation. *Bull. Amer. Meteorol. Soc.* **37**, 205–206.

Shuttleworth, W. J. (1991). Evaporation models in hydrology. *In* "Land Surface Evaporation: Measurement and Parameterization" (T. J. Schmugge and J.-C. André, Eds.), pp. 93–120. Springer-Verlag, New York.

Simard, A. J. (1968). "The Moisture Content of Forest Fuels—I." Inf. Rep. FF-X-14. Forest Fire Research Institute, Ottawa.

Sperry, J. S., and Pockman, W. T. (1993). Limitation of transpiration by hydraulic conductance and xylem cavitation in *Betula occidentalis*. *Plant Cell Environ.* **16**, 279–287.

Sun, J., and Mahrt, L. (1995). Determination of surface fluxes from the surface radiative temperature. *J. Atmos. Sci.* **33**, 1110–1117.

Tarpley, J. D. (1979). Estimating incident solar radiation at the surface from geostationary satellite data. *J. Appl. Meteorol.* **18**, 1172–1181.

Thom, A. S. (1975). Momentum, mass and heat exchange of plant communities. *In* "Vegetation and the Atmosphere, Vol. 1. Principles" (J. L. Monteith, Ed.), pp. 57–109. Academic Press, New York.

Thornthwaite, C. W. (1948). An approach toward a rational classification of climate. *Geogr. Rev.* **38**, 55–94.

Tyree, M. T., and Sperry, J. S. (1988). Do woody plants operate near the point of catastrophic xylem dysfunction caused by dynamic water stress? *Plant Physiol.* **88**, 574–580.

Van Wagner, C. E. (1987). "Development and Structure of the Canadian Forest Fire Weather Index System." Forestry Technical Report 35. Canadian Forestry Service, Ottawa.

Weiss, A. (1983). A quantitative approach to the Pruitt and Doorenbos version of the Penman equation. *Irrig. Sci.* **4**, 267–275.

Zeng, X., and Dickinson, R. E. (1998). Effect of surface sublayer on surface skin temperature and fluxes. *J. Climate* **11**, 537–550.

Zhan, X., Kustas, W. P., and Humes, K. S. (1996). An intercomparison study on models of sensible heat flux over partial canopy surfaces with remotely sensed surface temperature. *Remote Sens. Environ.* **58**, 242–256.

Zhong, M., Weill, A., and Taconet, O. (1990). Estimation of net radiation and surface heat fluxes using NOAA-7 satellite infrared data during fair-weather cloudy conditions of MESOGERS-84 experiment. *Boundary Layer Meteorol.* **33**, 353–370.

Zilitinkevich, S. S. (1970). "Dynamics of the Atmospheric Boundary Layer." Leningrad Gidrometeor, Leningrad.